Int. J. Ion Mobil. Spec. (2012) 15:199–222
DOI 10.1007/s12127-012-0109-x

ORIGINAL RESEARCH

Characterization of a miniature, ultra-high-field, ion mobility spectrometer

Ashley Wilks · Matthew Hart · Andrew Koehl · John Somerville · Billy Boyle · David Ruiz-Alonso

Received: 29 February 2012 / Revised: 14 June 2012 / Accepted: 22 June 2012 / Published online: 30 August 2012

Abstract By combining a multiple micron-gap ion separator with a novel high-frequency separation waveform drive topology, it has been possible to considerably extend the separation field limits employed in Field Asymmetric Ion Mobility Spectrometry (FAIMS)/Differential Mobility Spectrometry (DMS); giving rise to an *Ultra-High-Field* operational domain. A miniature spectrometer, based around the multi-micron-gap ion separator and ultra-high-field drivers, has been developed to meet the continuing industrial need for sensitive (sub-ppm), broadband and fast (second timescale) response volatile chemical detection. The packaged miniature spectrometer measures 12×12×15 cm, weighs 1.2 kg and is fully standalone; consisting of the core multi-micron gap ion separator assembly and RF/DC electronic drivers integrated with pneumatic handling/sample conditioning elements, together with ancillary temperature, flow and humidity sensing for stable closed loop operation (under local microprocessor control). The combination of multiple micron-gap ion separators with the novel high-frequency separation waveform drive topology enables ion separations to be performed over scanning electric field ranges of 0 to >75 kV·cm^{-1} (0 to >~320 Td at 101 kPa), offering a potential solution to trace and ultra-trace chemical detection/monitoring problems, that conventional IMS and DMS/FAIMS may otherwise find challenging. In this ultra-high field operational regime *effective ion temperatures* may be "swept" from ambient to >1000 K because *critically*, the effective ion temperature scales to at least the *square* of the applied field. With this field induced ion heating a controlled manipulation (or switching) of the ion chemistry *within* the separation channel (the ion drift region) may be invoked. For example, ion fragmentation via thermal dissociation can be induced. Chemical separation and identification is thus derived from the unique kinetic and thermodynamic behavior of ions assessed over a very broad effective temperature range. In addition to describing the novel miniature spectrometer, this paper addresses key aspects of ultra-high-field operation, which render it distinct from traditional ion mobility technologies and principles. In particular, this paper essays a model of ultra-high-field operation and highlights model deviations, whilst providing clear theoretical explanation backed up with experimental evidence.

Keywords FAIMS · DMS · Ultra-high-fields · Rapid thermal modulation · Ion kinetics · Miniature spectrometer

A. Wilks (✉)
Owlstone Inc.,
761 Main Avenue,
Norwalk, CT 06851, USA
e-mail: ashley.wilks@owlstoneinc.com

M. Hart · A. Koehl · J. Somerville · B. Boyle · D. Ruiz-Alonso
Owlstone Ltd,
127 Cambridge Science Park,
Cambridge CB4 0GD, UK

Introduction

Since its conception in the early 1980's [1] and first publication in the early 1990's [2] Differentially Mobility Spectrometry (DMS)/Field Asymmetric Ion Mobility Spectrometry (FAIMS) has become recognized as a useful tool in the separation and characterization of gas phase ions. Two clear and differentiable separator configurations have become well established; the cylindrical design [3] and the planar design [4] and the associated operational models for each of these core designs have been discussed in some detail, e.g. [5]. A broad range of specific applications of the technology (toward the solution of challenging chemical

and biochemical separation problems) have also been described. These include uses of the technology in stand-alone form, e.g. [6], hyphenated with Mass Spectrometry, e.g. [7, 8] and hyphenated with Gas Chromatography, e.g. [9–14]. A comprehensive technology applications review was given by Kolakowski and Mester [15] and significantly a comprehensive text dedicated to the fundamental science behind DMS/FAIMS was published 2 years later [16]. Since 2009 there have been numerous more works relating instrumental developments and applications (including; [17–25]), evolving both the fundamental scientific understanding of the technology and appreciation of its broader analytical utility.

The present authors have been developing DMS/FAIMS technology since 2004 and the result of this effort has been the realization of what can be shown to be a miniature spectrometer with a unique mode of operation. A significant aspect in technology realization has been the ability to drive a planar variant of DMS/FAIMS, at extremely high (*Ultra-High*) fields (>75 kV·cm^{-1}, >320 Td at 101 kPa). In the early days of development the effects of operating an ion separation system at these ultra-high-fields were not fully understood; it was believed that models applicable to DMS/FAIMS would directly extend and be sufficient for spectral prediction/interpretation. Detailed data analysis and theoretical work has since revealed that the traditional model approximations breakdown; in particular the truncated form of the α-function, describing the field dependence of ion mobility, is no longer effective. This is thought to be largely due to the extremely high *effective ion temperatures* (T_{eff}) generated at ultra-high-fields, given that T_{eff} scales to at least the square of the applied field.

On the basis of our up-to-date understanding, present DMS /FAIMS model approximations do not adequately represent the separation principles when operating at ultra-high fields. Importantly, the kinetics and thermodynamics of ions *within* the separation region are fundamental drivers in the separation and identification process and these are manipulated by a rapidly scanning electric field. The scanning electric field enables effective ion temperatures to be evaluated from ambient to >1000 K on single-second timescales. Chemical separation and identification is ultimately derived from the unique kinetic and thermodynamic behavior of an ion that is generated from the analytical sample. Specifically, information relating to the *field dependent mobility* and *fragmentation pattern* of individual ions may be extracted and utilized in chemical classification.

In introducing the model of operation it is necessary to start with a discussion of the principles of electric-field-based gas-phase ion separations and in particular the well-established concept of *ion mobility* in a neutral drift gas. The miniature spectrometer described herein utilizes an oscillating electric field and does therefore have clear parallels with conventional DMS/ FAIMS operating at lower applied fields (<35 kV·cm^{-1}, ~150 Td at 101 kPa, 101.3 kPa.). It is thus essential to provide an overview of DMS/FAIMS based separation principles before expanding the discussion to incorporate the principles and differentiators associated with ultra-high-field operation that ultimately define the unique model of operation.

Foundations

Under standard conditions (101.3 kPa and 293.15 K) and in a *low electric field* (<5 kV·cm^{-1}) the mobility coefficient (K, m^2·V^{-1}·s^{-1}) of a singly charged ion, in a neutral drift gas, is principally governed by its reduced mass μ (kg) and collisional cross section Ω (m^2). K can be *approximated* by the well-known Mason-Shramp equation [26], where e is the elementary charge constant (~1.602×10^{-19} C), T_{eff} the gas temperature (K), k_b Boltzmann's constant (J·K^{-1}) and N the molecular density of neutrals in the gas (the drift gas) supporting the ion (2.503×10^{25} m^{-3})—

$$K = \frac{3e}{16N}\cdot\left(\frac{2\pi}{\mu k_b T}\right)^{\frac{1}{2}}\cdot\frac{1}{\Omega} \tag{1}$$

Under increasing (but *sub*-ultra-high-) field conditions the local temperature (or *effective temperature—*T_{eff}) of the ion begins to rise and can no longer be approximated to the gas temperature. With this increase in temperature the cluster ion is modified, it may expand (via the thermal population of rotationally and vibrational excited states) or contract (through the loss of a neutral entity, e.g. a weakly dipole- or induced-dipole-bound *solvent* molecule derived from the drift gas). This will lead to a modification of the collisional cross-section parameter (Ω). At these higher applied fields, Ω is replaced by the *effective-ion-temperature* dependent collisional cross-section parameter (Ω(T_{eff})) and the gas temperature T by T_{eff} (Eq. 2).

$$K(T_{eff}) \approx \frac{3e}{16N}\cdot\left(\frac{2\pi}{\mu k_b T_{eff}}\right)^{\frac{1}{2}}\cdot\frac{1}{\Omega(T_{eff})} \tag{2}$$

At constant N (i.e. gas constant pressure) the mobility coefficient K is thereby electric field dependent by virtue of the influence of the electric field on T_{eff} and K is therefore molecular specific on the basis of its dependence on Ω. This phenomenon is exploited for molecular separation and identification in DMS/FAIMS based systems. By passing an ionized gas through the gap between a pair of electrodes, over which an oscillating *asymmetric* electric field is applied, the mobility of the ion will oscillate between a low-field mobility K_0 (which may be approximated to be representative of the *reduced mobility coefficient* (K_0) i.e., the mobility at an applied field of low magnitude, where $T_{eff} \approx T$) and a high-field mobility K_E. The change in K (ΔK)

occurring in the high-field portion of the asymmetric waveform is a result of a high-field influence on T_{eff} and $\Omega(T_{eff})$.

Field dependence of K

At Standard Temperature and Pressure (STP) the field dependency of K_E (at least to an *approximation* over a *moderate* field range i.e., ~0–35 kV·cm^{-1}) may be related to the low-field mobility K_0, through Eq. 3, whereby α is the function of the K_E/K_0 *versus* E curve, e.g. [16, 27].

$$K_E = K_0[1 + \alpha(E)] \tag{3}$$

The α-function is polynomial expandable in even powers (Eq. 4), where the coefficients α_2, $\alpha_4 \ldots \alpha_n$, are specific to the ion, and more importantly the parent molecule (or molecular fragment) forming the ion.

$$K_E = K_0\left[1 + \alpha_2 E^2 + \alpha_4 E^4 \ldots + \alpha_n E^{2n}\right] \tag{4}$$

Under the aforementioned moderate field ranges the high-order terms can usually be neglected since they are of diminishing significance (in the realms of experimental precision) and Eq. 4 can be truncated to the fourth order—

$$K_E = K_0[1 + \alpha_2 E^2 + \alpha_4 E^4] \tag{5}$$

Since DMS/FAIMS systems utilize a non-perfect square waveform to drive the oscillating field (Fig. 1), it is extremely important that E is accurately defined. E is the *zero-to-peak* amplitude of the electric field generated by a waveform of zero-to-peak voltage (V_D) across electrodes of gap separation g (cm^{-1}). This is referred to as the *Dispersion Field*—E_D (kV·cm^{-1}).

This variable field definition is very important since the assumption that K_0 is representative of the low-field mobility does not hold up well at very high fields (where the field across the separation electrodes will actually be significant in the "low field" portion of the applied asymmetric field). This is potentially one of the aspects of ultra-high-field operation that distinguishes it from variants of FAIMS/DMS, which operate over a lower range of E_D (~0–35 kV·cm^{-1} c.f., 0–75 kV·cm^{-1}) and absolutely stresses the approximations associated with the truncation of the α-function to only the fourth order. We shall go on to evaluate this aspect throughout this paper.

The α-coefficients in Eq. 5 are very small relative to E (~10^{-5}, ~10^{-9} respectively) and may be *positive* or *negative* in sign. The ratio K_E/K_0 may therefore be >1 or <1, reflecting the fact that the high-field mobility $K(E)$ may be less than, or greater than, the low-field mobility at various points across the K_E/K_0 *versus* E curve. By the same token we can say that ΔK (defined as K_E–K_0) is positive in sign when the high-field mobility exceeds the low-field mobility and negative in sign when the opposite is the case. For low and medium molecular weight species (e.g. volatile and semi-volatile organic compounds of molecular weight <~300 g·mol^{-1}) ΔK will typically range from 0 % to 10 % of the low field mobility (K_0) and this should be kept in mind (i.e. the differential mobility is *small* relative to low- or high-field mobility).

In *rough* terms, a positive ΔK is observed when the ion "shrinks" (i.e. the Ω decreases) on the transition between the low-field and high-field portion E_D, while a negative ΔK is observed when the ion "expands" (i.e. Ω increases) on the transition. The $\Omega(T_{eff})$ function is very nonlinear and is dependent on a variety of molecular specific physical and chemical properties (e.g. ion clustering/declustering kinetics and the efficiency of energy transfer during ion-neutral molecular collisions). As such, the *sign* of ΔK can change with increasing E_D.

Separation mechanism

Post ionization, ions are transported transversely (perpendicular to the applied field) through the separator electrodes in a uniform gas flow. At constant E_D the ΔK induced by the oscillating asymmetric field manifests as alternation of the longitudinal (parallel to the field) drift velocity (v_D, cm·s^{-1}) between the high-field portion of the applied waveform (of a duration τ, s) and low-field portion of the applied waveform (of a duration t, s). This is illustrated in Fig. 2.

The longitudinal drift velocity is given by the relation $v_D = K \cdot E$. When $K_E > K_0$, v_D will be higher (and the longitudinal distance covered by the ion greater) in the high-field portion of the applied waveform. Conversely, it will be lower (and the longitudinal distance covered by the ion less) in the low-field portion of the applied waveform. When $K_E < K_0$ the opposite will apply. Simply, the direction of the longitudinal drift will depend on the sign of ΔK; the net drift being in the direction of one separator electrode when ΔK is positive in sign and toward the opposite electrode when ΔK is negative in sign. At a given E_D, only ions of $\Delta K = 0$, or else those whose drift velocities are matched such that the longitudinal high-field drift path length d_h (cm) is equal to the longitudinal low-field drift path length d_l[1], will be carried fully parallel to the gas flow and detected (Fig. 2). Other ions will be neutralized on the separator electrodes. Clearly, the condition where $\Delta K = 0$ (i.e. $K_E/K_0 = 1$) is very precisely field dependent (as Fig. 2 illustrates) and only true at relatively high, or else very low, E_D. Nevertheless, *subtly* tuning E_C (~±5 %) around a given E_D set point will be sufficient to offset any net longitudinal drift experienced by an ion of a given ΔK. This tuning field is referred to as the *Compensation Field* (E_C) and in

[1] Through the relation $d_h = v_{D(h)} \cdot \tau$ and $d_l = v_{D(l)} \cdot t$, where $v_{D(h)}$ are $v_{D(l)}$ are the respective high- and low-field drift velocities

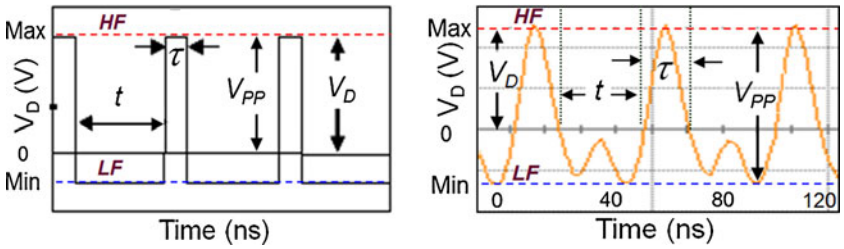

Fig. 1 **a** Idealized square rectangular waveform and actual waveform (**b**) whereby *HF* and *LF* respectively represent the high field and low field portion of the applied field. The Dispersion Field (E_D) is defined by the zero-to-peak voltage of the applied waveform (V_D) across the electrodes that form the ion separator (see also Fig. 2)

sweeping E_C, ions are selectively filtered on the basis of their ΔK. Further, since ΔK exhibits molecular specificity and is a strong function of E_D, the ion current output obtained when stepping E_D in combination with a sweeping E_C offers a highly molecular-selective output. This E_C:E_D output is the *Dispersion Spectrum*, which will be familiar from DMS/FAIMS.

Standardization of electric field to E/N

The mobility co-efficient K is pressure dependent by virtue of the $1/N$ dependency in Eqs. 1 and 2. Normalization with respect to pressure is therefore essential to overcome the effects of natural meteorological and altitude variations and E ($V{\cdot}m^{-1}$) is replaced with E/N ($V{\cdot}m^2$). The importance of this has been explicitly discussed by Nazarov et al. [28]. At STP (101.3 kPa and 295.15 K) N (m^{-3}) is very large (2.503×10^{25} m^{-3}) and E/N and very small ($\sim10^{-19}$ $V{\cdot}m^2$ at E=200 $kV{\cdot}cm^{-1}$ under the same STP condition). A more convenient unit in E/N expression, for spectral representation, is the Townsend (Td), where 1 Td=10^{-21} $V{\cdot}m^2$.

Logistics of ultra-high field operation

Operation at ultra-high-fields requires the use of very narrow-gap (micron-scale) ion separators (Fig. 3), in order to relax the engineering challenges associated with waveform driver design [29]. Minimizing this gap ultimately enables higher fields to be generated with lower voltage and smaller form-factor waveform drivers. That said; waveform driver development requires an exceptional appreciation for magnetic circuit design. The development of high-

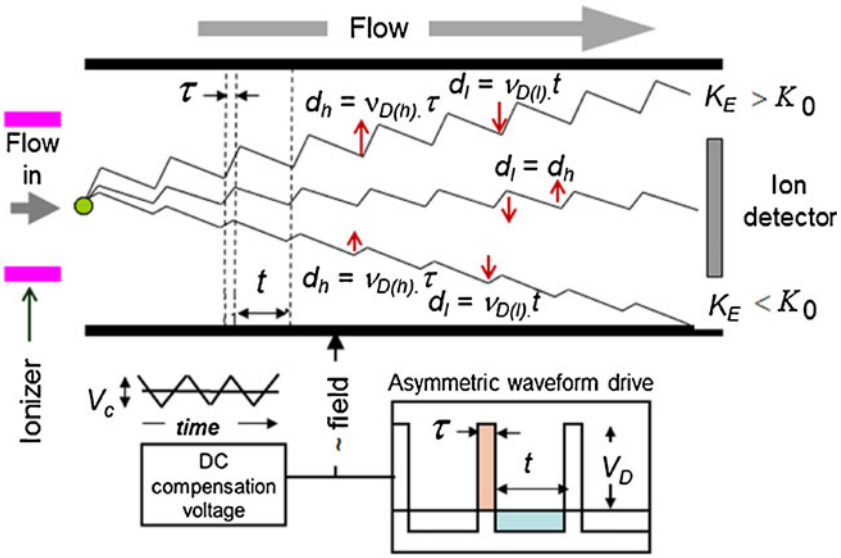

Fig. 2 Ion Drift in an oscillating electric field. A variable high-voltage asymmetric waveform of low-voltage-pulse duration t (s) and high-voltage duration τ (s) and peak voltage V_D is applied between electrodes of gap g (cm), creating a variable Field of V_D/g ($kV{\cdot}cm^{-1}$), through which ions oscillate and adopt a net longitudinal drift path length (d_h–d_l), which is determined by their high- and low-field drift velocity ($v_{D(h)}$ and $v_{D(l)}$) and the high field/low field pulse duration. A bias DC "tuning voltage" (V_c) applied on top of the applied waveform enables subtle adjustment of V_D to counter the drift experienced by an ion of a specific ΔK, where ΔK is the difference between the high field ion mobility (K_E) and low field ion mobility (K_0)

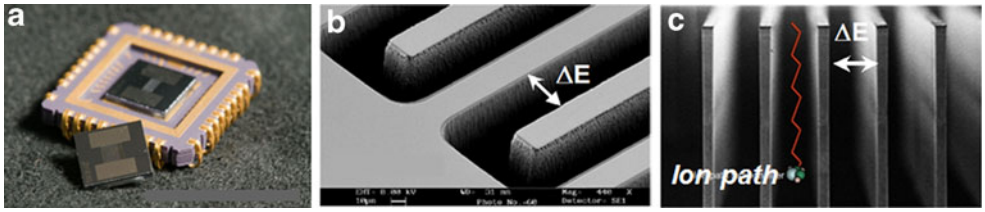

Fig. 3 The "inter-digitated" micro-fabricated ion separator utilized for ultra-high-field operation (based on a design first presented by Boyle et al. [29]). **a** Etched ion separator in sensor package, **b** Magnification of sensor surface showing serpentine ion separator channels (of 35 μm separation gap), **c** Simulation of cross-section through senor showing parallel separation channel arrangement (with schematic of ion passing through a channel overlaid where ΔE denotes the applied field)

voltage, high-frequency asymmetric waveforms, with a "size and power" optimized topology, has in some respects been a beyond state-of-the-art exercise and this paper therefore strives to articulate an unambiguous separation waveform analysis.

Use of such narrow gaps also warrants the use of short ion separation channels and substantially higher asymmetric waveform frequencies, as compared to those employed in a larger-gap design; such as described by Krylov et al. [30], (300 μm c.f. 1 cm and 27 MHz c.f. 1 MHz respectively). Short ion separation channels must be employed in order to maximize ion transmission, and high waveform frequencies must be employed such that a sufficient number of ion oscillations may occur (in a short ion separation channel) to promote ion separation, as has been discussed by Shvartsburg et al. [31]. The combination of high frequency and short channels means that ion-molecule collisions are minimized in the low field (LF) and high field (HF) period of the applied waveform (between which, ion-chemistry is manipulated) as well as in the short timescale (μs) transit through the channel (Fig. 4). This has some profound effects on ion chemistry, since separation timescales become more comparable to natural ion-neutral collision frequencies at atmospheric pressure (~5 GHz). Short-lived ion fragments generated *within* the ion separator may therefore be observed and utilized in classification, as we shall go on to discuss later in this paper.

Instrumental specifics

The ion separator (as was illustrated in Fig. 3) consists of 27 ion channels of gap width (g)=34.5 (±0.2) μm[2] and length (L)=300 (±5) μm. It is fabricated by etching a 37 mm long serpentine channel into a silicon wafer to form a 1.2 mm^2 open area. The gap surfaces are made of high-conductivity silicon and are electrically connected via wire bonding to metal pads on the face of the silicon. The chip is packaged and mounted onto a bespoke high-temperature co-fired ceramic (HTCC) package.

The asymmetric waveform is synthesized using a proprietary Radio Frequency (RF) circuit design. The RF output contains significant higher-order terms but can be approximated by 2 sinusoids—a fundamental and its first harmonic. The first harmonic is 1/2 the amplitude of fundamental and 90° out of phase, yielding a waveform described by the function:

$$V(t) = \sin(\omega_1 t) + 0.5\cos(\omega_2 t) \quad (6)$$

Where ω_1 and ω_2 are the angular frequencies of the fundamental and first harmonic, respectively, and V is the voltage (V). A digital oscilloscope recording of the waveform as applied across the ion separation electrodes was shown in Fig. 1(b).

The amplitude of the waveform in the high-field segment (V_D) is variable up to ~250 V corresponding to a dispersion

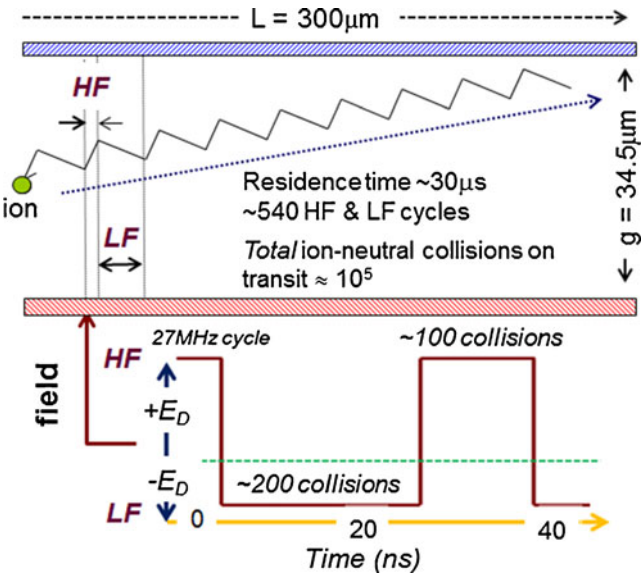

Fig. 4 Schematic representing ion transport through the ion separator shown in Fig. 3. Ion–neutral collisions (of ~5 GHz in frequency) during each high-field (HF) and low-field (LF) cycle, at operational pressure (~100 kPa), are relatively few

[2] The ion filter has a manufacturing specification in the channel width of 35±0.6 μm. The measurement tolerance on the channel width after manufacture is 0.2 μm.

field (E_D) range of 0–75 kV·cm^{-1} (equivalent to E_D/N= 0–320 Td under standard atmospheric operational conditions, 101.3 kPa). The addressable E_D resolution is 14 V·cm^{-1} corresponding to E_D/N=61 mTd under the same conditions and may be stepped at rates of up to 10 *divisions per second* parallel with the "tuning" *compensation field* sweep (E_C).

E_C is generated by a DC voltage superimposed on the asymmetric waveform as was illustrated in Fig. 2. The DC voltage may be swept in a range of ±8 V with <2 mV addressable resolution at a rate of 1.3 ms·step^{-1}, yielding an E_C of ±2.3 kV·cm^{-1} and <1 V·cm^{-1} resolution (equivalent to E_C/N±10 Td, with 2 mTd resolution under standard atmospheric pressure operational conditions). A sweep of ±6 Td more than adequately suffices (as one approaches maximum E_D/N) for volatile and semi-volatile compounds (MW<350 AMU).

Ions are carried through the ion separator in air at ambient pressure. The ion source is a custom designed corona discharge that generates both positive and negative ions. The ion separator may be heated in a range of ambient to 60 (±1)°C and is monitored/stabilized by means of a temperature sensor (TC74A5-5.0VAT; *Microchip Inc, Chandler, AZ*) in feedback loop with the heater controller. The inlet sample may be diluted in a ratio ranging from 3:1 to 30:1 in a recirculating dry and purified air flow, whereby the air exiting the ion separator is purified through an activated charcoal and molecular sieve "scrubber" with integrated particulate filter. The standard flow rate through the ion separator is 380 (±10) cm^3·min^{-1} and the sample inlet to diluent flow ratio is controlled by a variable solenoid valve at the outlet of the sensor assembly (where the sensor assembly is defined as an assembly of the ion source, ion separator package, ion detector and ancillary sensing devices, Fig. 5). An exhaust solenoid placed in front of the variable solenoid allows for complete air recirculation (i.e. shut-off of the inlet sample flow) providing protection from

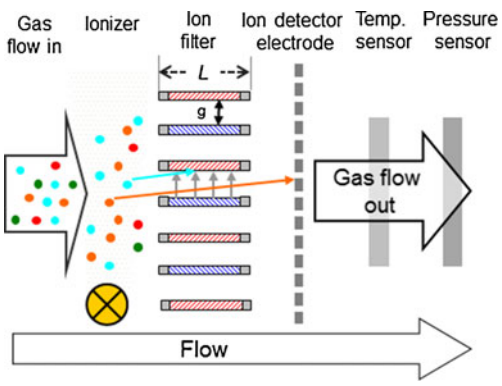

Fig. 5 "Sensor head" arrangement of the miniature spectrometer (described in text and in Fig. 6). *L* represents the separation channel length (300 μm) and *g* the separation channel gap (34.5 μm) across which the *dispersion field* (E_D) and *compensation* field (E_C) is applied

contamination scenarios. Air is pulled through the sensor assembly by means of a rotary vane pump. A temperature and pressure sensor (BMP085; *Bosch, Gerlingen, Germany*) is mounted at the exit of the sensor assembly to accurately monitor the gas temperature and pressure. A humidity and temperature sensor (SHT15: *Sensirion AG, Stäfa, Switzerland*) is mounted at the sample inlet to monitor these ambient (environmental) variables (Figs. 6 and 7)

The ion detector electrode consists of a gold plated hexagonal grid of 6×0.5 mm holes positioned 1 mm after the chip and biased at ±30 V on alternating sweeps of E_C for cation and anion detection. The ion current impacting the electrode is measured by a Transimpedance Amplifier (TIA). As standard a E_C sweep time of 420 ms with 400 E_C steps, yields a sampling time of approximately 1 ms·step^{-1}. Ion current response data is passed to a local processor (ARM 7- TDMI, *Texas Instruments, Dallas, TX*), which serves also to set spectral acquisition parameters (E_C range, E_D range, step size, etc.). High-level systems control is performed by a laptop PC (*Latitude E5500; Dell Inc, Round Rock, TX*), with a custom control/data acquisition user interface (*LabVIEW 8.5; National Instruments, Austin, TX*) which is linked by USB to the local processor. This user interface also serves to present spectral data in real time and log data for offline analysis.

Separation waveform analysis

As was noted in the introduction, the generation of a high-voltage, high-frequency asymmetric waveform is non-trivial. RF circuits are inherently non-linear, so the separation waveform applied across the ion separator must be well characterized through the operational field range. The waveform employed by the authors closely matches the sum of 2 sinusoids described by Eq. 6 but is non-ideal. The peak waveform voltage is not a linear function of the bias applied to the RF oscillator (*or, more specifically, the equivalent circuit formed by the RF circuit coupled to the ion separator*) and the precise function of the waveform exhibits some dependence on this bias voltage. Comparisons against a FAIMS/DMS model can only be made with clear quantification of critical waveform parameters through the operational field range. These critical parameters are; *i*) the power (and thus *V*) transfer function—$V_p(V_b)$, *ii*) the peak voltage vs. frequency response—$\omega(V_p)$ and *iii*) the precise function of the waveform—$f(t)$. The importance of *i*) is automatically realized through inspection of Eq. 3 and the importance of *ii*) can be rationalized (when considering also the ratio of HF and LF period) in terms of its impact on ion kinetics in the HF and LF segment of the applied waveform. The importance of *iii*) is less straightforward but a mathematical description has been widely discussed [5, 32, 33]. This description reduces the separation waveform to a series of

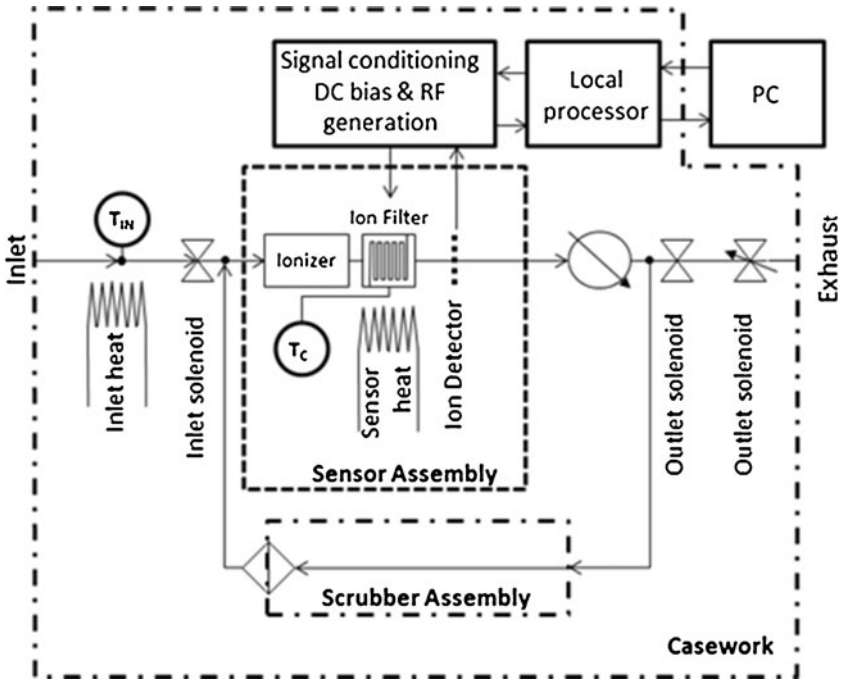

Fig. 6 The miniature spectrometer; system diagram

coefficients which help define the E_C:E_D spectrum for a given ion, in a separation field derived from a waveform of function $f(t)$. The waveform coefficients are defined as—

$$\langle f_n \rangle = T^{-1} \cdot \int_0^T f_n(t)dt. \quad (7)$$

where T is the period of the waveform (i.e., $t + \tau$ in Fig. 2). In the field dependence of ion mobility approximated by Eq. 4 the lower-order coefficients $<f_2>$, $<f_3>$ and $<f_5>$ are of specific importance.

All critical waveform parameters have been evaluated through assessment of the waveform as measured across the serpentine assembly of ion separator electrodes. The waveform was recorded at a range of oscillator bias voltages using a high-sample-rate digital storage oscilloscope and impedance-matched coupling probe. The *peak* and *minimum* waveform voltages, as a function of the drive voltage, were then derived to obtain the drive voltage to RF output voltage transfer function, before subsequently deriving the separation waveform coefficients $<f_2>$, $<f_3>$ and $<f_5>$ and also the $\omega(V_p)$ dependencies. The data are summarized in Figs. 8 and 9.

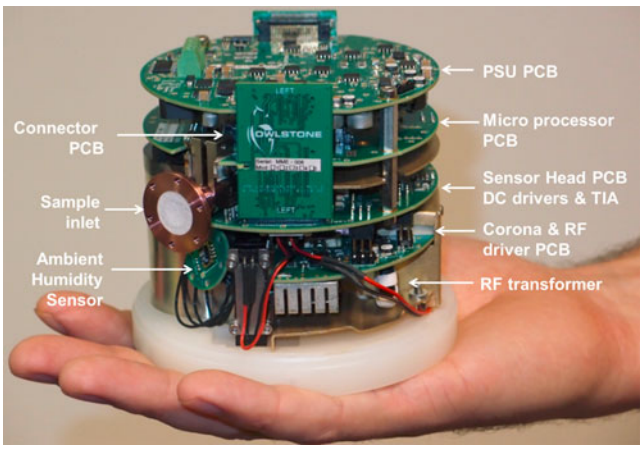

Fig. 7 Photograph of Hardware layout excluding case work with visible parts annotated. The "scrubber assembly slots into the base and the pump is located at the exhaust assembly (reverse side of view shown here). A systems diagram was shown in Fig. 6

The $V_P(V_b)$ response (Fig. 8) could be closely approximated to a 3rd order polynomial, with measurement uncertainties scaling roughly with V_b. These were ~±2.5 % RSD, except at the lowest V_b setting at which measurements were taken, where an RSD of ~ ±10 % was observed. It is to be noted that accuracy in V_p is less critical at the very low end of the scale, since at low E_D/N (<25 Td) ion peaks are only partially resolved. On this basis one could conclude that the V_p of the waveform was quantitatively characterized for precise E_D/N scaling.

The $\omega(V_p)$ response (Fig. 9a) was effectively constant (given measurement uncertainties) across the working V_p range. Taking the mean of all measurements the waveform frequency was defined as 27.15 (±0.04) MHz. More interesting were the derived $<f_n>$ waveform coefficients, which account for departures of the waveform function from Eq. 6 (due to the presence of higher-order terms). The coefficients were well defined at any single V_p but varied across the working V_p range. These coefficients ranged from 0.1918–0.2348, 0.0634–0.1073 and 0.0654–0.1052, for $<f_2>$, $<f_3>$ and $<f_5>$ respectively. At

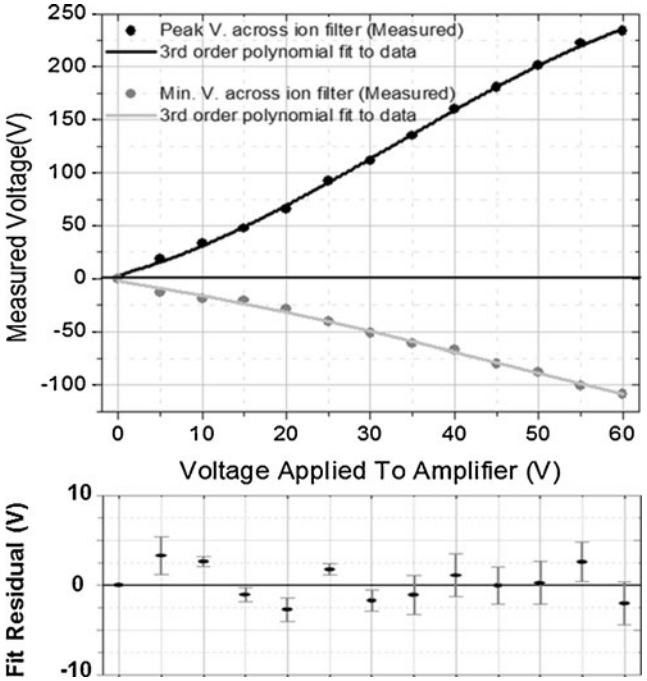

Fig. 8 **a** Measured peak (black data points •) and minimum (*grey data points* •) waveform voltages as a function of RF waveform generator drive voltage. The peak and minimum voltage transfer functions closely fits a 3rd order polynomial, $y=a+bx+cx^2+dx^3$, where constant a is fixed to 0V (R^2>0.999). **b** Residual data (obs—fitted) for the *peak* waveform voltage, where error bars are the standard deviation for *three* replicate measurements across the serpentine assembly of ion separator electrodes

the minimum V_p measurement point the measured $\langle f_3 \rangle$ and $\langle f_5 \rangle$ coefficients deviated most from the mean values and these points were dropped from the final mean $\langle f_n \rangle$ calculations. The $\langle f_2 \rangle$, $\langle f_3 \rangle$ and $\langle f_5 \rangle$ coefficients were thereby defined as 0.2134 (±0.0160), 0.0967 (±0.0048) and 0.0879 (±0.0070). The validity of using averaged across operation field range $\langle f_n \rangle$ values in spectral evaluations is addressed in "Ion peak position".

Definition of Ion residence time

A firm definition of the ion residence time (t_{res}) within the ion channel is required in order to perform effective systems validation. The gas flow through the ion channel is laminar (parabolic). Ions are only detected when $\nu_{D(h)} = \nu_{D(l)}$ (c.f. Fig. 2) and these ions emanate from the center of the ion channel. Under a laminar flow condition the maximum flow velocity (v_{max}, m·s^{-1}) occurs at the center of the ion channel, whilst the minimum flow (v_{min}) velocity occurs at the edges. The average flow velocity (v_{Av}) is defined as Q/A, where Q is the gas flow rate (m^3·s^{-1}) and A the surface area of open flow channels (m^2). In a macro-circular channel v_{max} (under a laminar flow condition) is easily defined by the expression $2Q/A$. For a rectangular (planar) micro-channel, however this relationship does not hold. Indeed, the accurate determination of v_{max} is an involved process [34]. A reasonable approximation can nevertheless be made by integrating the equation which defines the flow velocity (v_x) at any point (x), between the extremes $\pm x$, through the cross-section of the ion channel; i.e., $v_x = v_{\max}(1 - x^2)$. Doing so one derives the expression $v_{\max} = \frac{3}{2} \cdot v_{Av}$, i.e., the maximum flow velocity defining t_{res} is 1.5 that of the average flow velocity and t_{res} is given by the expression—

$$t_{res} = LA/(1.5 \cdot Q) \quad (8)$$

Based on our open channel area of 1.17 mm^2, channel length of 300 μm and a typical operational flow rate of 350–400 cm^3·s^{-1} this yields an ion residence time of ~30–40 μs.

Model of operation

The spectral output (the *Dispersion Spectrum*) is analogous to that observed in conventional DMS/FAIMS in so far as it consists of an $m \times n$ matrix of ion current measurements at m compensation field (E_C/N) and n dispersion field (E_D/N)

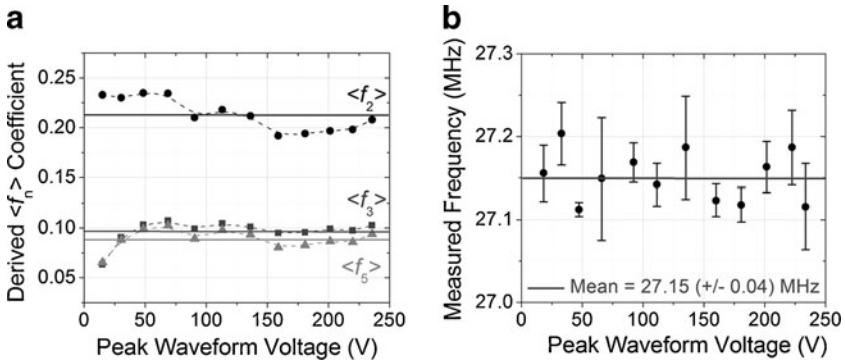

Fig. 9 **a** Measured Waveform frequencies across peak waveform voltage range (uncertainties represent standard deviations, n=3). **b** Waveform coefficients $\langle f_2 \rangle$ (black data points •), $\langle f_3 \rangle$ (*dark grey data points* •) and $\langle f_5 \rangle$ (light grey data points •) across peak waveform voltage range derived from the observed waveform, (errors for n=3 measurements relating each peak waveform voltage point were <0.005, i.e., <5 % RSD)

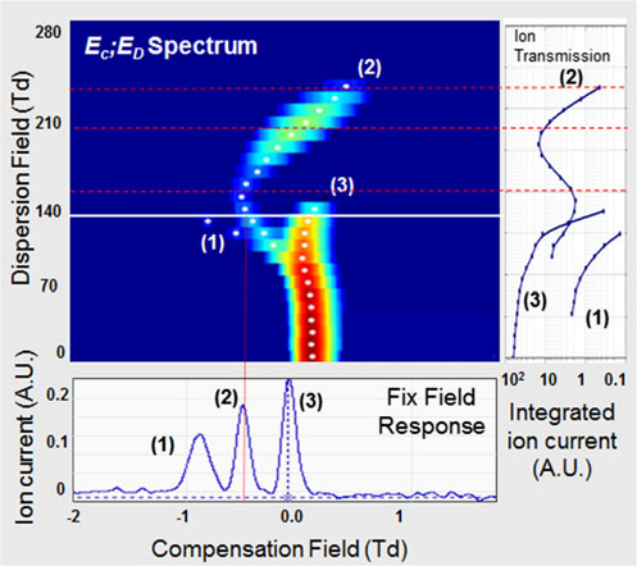

Fig. 10 The E_C:E_D spectrum represents the ion current at the output of the ion separator as a function of the Compensation Field (E_C/N) and the Dispersion Field (E_D/N). The Ion Transmission spectrum represents the integrated ion current for each resolved peak as a function of E_D

settings (Fig. 10). A spectral peak at fixed E_D/N can be characterized by its Gaussian parameters, i.e., position (E_C/N), height (I) and width (w). The E_C:E_D spectrum, which is the evolution of Gaussian response as a function of E_D/N, can be characterized by the derived Gaussian parameters. A dense E_C:E_D spectrum may be obtained on single second timescales because ion separation times are short (~30 μs). The E_C:E_D spectrum is viewed holistically in deriving information about the analyzed sample and performing chemical classification.

In discussing the model of operation it is helpful to establish a foundation based on the DMS/FAIMS model and then to build upon this. DMS/FAIMS models are well established and provide an invaluable point of reference in the lead up to the discussion of ultra-high-field operation. The work of Guevremont [5], Krylov et al. [32] and Shvartsburg [16] is fundamental in the discussion that follows.

Ion peak position

At lower E_D/N (<140 Td) it may be shown [32] that the peak position (E_C/N) may be *approximated* by considering the field dependency of the ion–mobility coefficient (described by the alpha-function, Eq. 5) and the *Dispersion Field* amplitude (E_D/N) by the relation—

$$E_C/N = c_3(E_D/N)^3 + c_5(E_D/N)^5 \tag{9}$$

in which the constants c_3 and c_5 are given by—

$$c_3 = \alpha_2\langle f_3\rangle \tag{10}$$

$$c_5 = (\alpha_4\langle f_5\rangle) - (3c_3\alpha_2\langle f_2\rangle) \tag{11}$$

and $\langle f_2\rangle$, $\langle f_3\rangle$ and $\langle f_5\rangle$ are *separation waveform coefficients* dictated by the function of the waveform from which the scanning E_D/N is generated. These waveform coefficients were defined, for the waveform employed by the present authors, in "Separation waveform analysis". On this basis, a *simulation* of the E_C:E_D spectrum is possible given a knowledge of the α_2 and α_4 parameters. The inverse problem is solvable; i.e., α_2 and α_4 parameters may be derived from a statistical fit of Eq. 9 to the empirical spectral data, given knowledge of the $\langle f_2\rangle$, $\langle f_3\rangle$ and $\langle f_5\rangle$ separation waveform coefficients.

It may be recalled from "Separation waveform analysis" that the waveform coefficients show some deviation across the V_p range. In data evaluation the *mean* values are used. The validity of this requires consideration, given that the peak position is dependent on these coefficients. To evaluate this we model the E_C:E_D response for the acetone monomer and dimer using the *minimum*, *mean* and *maximum* values for each of the derived coefficients recorded in Fig. 8b (ignoring the data points at V_p=11V). The result is shown in Fig. 11. Whilst we do see some offset at any fixed E_D/N, it should be remembered that there is already a marginal uncertainty in the dispersion field (~ ±2 %) from the $V_p(V_b)$

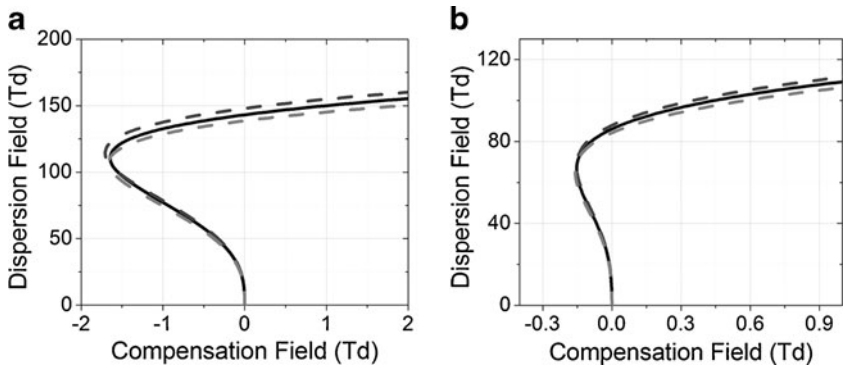

Fig. 11 **a** and **b** Simulated E_C:E_D responses for the acetone monomer (**a**) and dimer (**b**) using the minimum, mean and maximum values for each of the derived f_n coefficients recorded in Fig. 8b. *Black lines* (—) are the mean, *light grey dashed lines* (----) are the minimums and *dark grey dashed lines* (----) the maximums. The α_2 and α_4 coefficients used in spectral simulation were taken from Krylov et al. [35]

transfer function (Fig. 9). On this basis, any offset introduced from uncertainties in the waveform coefficients can be considered relatively insignificant.

Limitations of the truncated form of the α-model and Ion breakdown at high-field

The problem with the truncated form of the α-function (Eq. 5) is that it is only holds at lower E_D/N (<150 Td). At higher E_D/N the truncated model predicts that the peak E_C/N position → E_D/N (Fig. 11), whereas real ions do not behave as such (e.g. Fig. 12). Comparisons of Figs. 11 and 12 indicate that at higher E_D/N there is a need to retain higher order α terms, as shall be addressed in "Validation and discussion: observed vs. theory". It is also necessary to consider that the K_E/K_0 *versus* E/N curve (described by the α-function) is not continuous, since ions will undergo structural breakdown at sufficiently high-field. Appreciation of why this is the case requires a detailed consideration of the ion chemistry within the ion separator, in particular the *kinetic* and *thermodynamic* impacts resulting from the highly non-linear dependency of effective ion temperature (T_{eff}) on E_D/N. This is explored in "Ion peak intensity", which addresses ion transmission and peak intensity.

Ion peak intensity

Understanding the relationship between E_D/N and the ion peak intensity requires a combined consideration of *1*) ion transmission through the separator (dictated by the drift gas flow rate, molecular ion diffusion and the combined length/width of the ion separation channel) and *2*) ion chemistry in the ion separator. The former is easier to address since it has been well defined for the *lower field* (DMS/FAIMS) case by Krylov et al. [32].

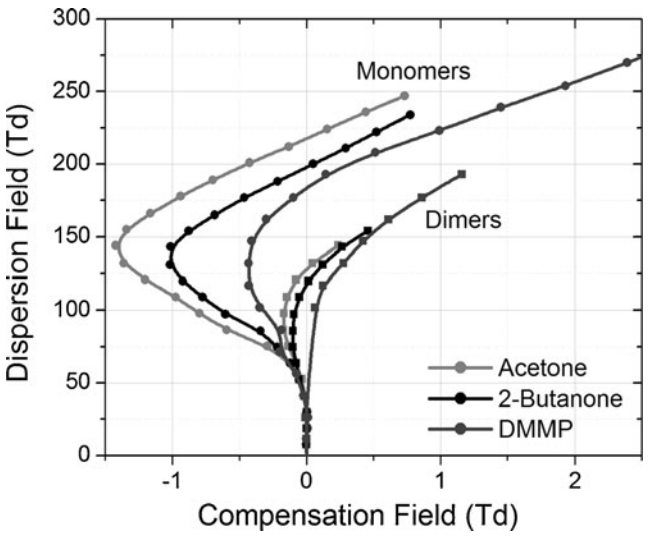

Fig. 12 E_C:E_D peak trajectories for monomer and dimers of acetone (*light grey data* points ●, ■), 2-butanone (*black data points* •, ■) and Dimethyl, Methyl Phosphonate (*dark grey data points* ●, ■) obtained experimentally using vapor concentrations of ~1 ppm by volume at ~10 ppm by volume H_2O. Note: *lines* (—) are point by point beta-spline connectors through the data and serve only as a guide to the eye

Lower field range (<150Td)

The multi-channel ion separator described in "Instrumental specifics" is effectively an assembly of 27 parallel planar electrodes and the ion density distribution within the ion separation channels fits the "weak focusing" case described by Krylov et al. [32]. However, the analysis of those authors rationalizes in terms of peak height since for the planar ion separator they describe, the peak width could be reasonably approximated as being independent of E_D/N. In the case of the multi-channel ion separator described by the present authors, the peak width exhibits a dependence on E_D/N (as shall be explained in "Peak width"). As such peak height must be substituted for peak area (integrated ion current), which is independent of broadening effects encountered across the E_D/N scan range.

The integrated peak ion current (A_I) will be a fraction of the "averaged over cross-section" input integrated peak ion current, $A_{I(in)}$. In the *weak focusing* case A_I may be approximated through the Equation—

$$A_I = A_{I(in)} Q \cdot \exp\left(-t_{res}\pi^2 D_{II}/g_{eff}^{\ 2}\right) \tag{12}$$

where Q is the gas flow rate ($m^3 \cdot s^{-1}$), t_{res} the ion residence time in the ion separator (s), D_{II} the *anisotropic* ion diffusion coefficient ($m^2 \cdot s^{-1}$) and g_{eff} the effective gap width (m).

g_{eff} is smaller than the physical gap width (g) and corrects for the longitudinal (*parallel to the applied field*) displacement of an ion during a HF (d_h) or LF (d_l) waveform cycle (Fig. 4), noting that at the ion peak d_h=d_l. Using g_{eff}=g−d_l and (recalling from "Introduction") that $d_{(l)} = \upsilon_{D(l)} \cdot t$ and $\upsilon_{D(l)}$=$K_0 E_{min}$, g_{eff} is defined by—

$$g_{eff} = g - (K_0 E_{min} t) \tag{13}$$

where E_{min} ($V \cdot m^{-1}$) is the *average* field across the ion separator in the duration of a LF cycle of the E_D/N waveform. g_{eff} is thereby proportional to $1/E_{min}$, across the scanning E_D/N range. Figure 13 shows that for a typical ion of $K_0 \approx 1.8 \times 10^{-4}$ $m^2 \cdot V^{-1} \cdot s^{-1}$, this scales from g_{eff}=g (i.e., 35 μm) at E_D=0 $kV \cdot cm^{-1}$, through $g_{eff} \approx 25$ μm at the near maximal E_D of 75 $kV \cdot cm^{-1}$ (i.e., $E_{min} \approx 18$ $kV \cdot cm^{-1}$, based on the waveform described in Eq. 6); noting that g_{eff} is strictly dependent on the field strength E ($V \cdot m^{-1}$), as opposed E/N ($V \cdot m^2$).

The other field-dependent term in Eq. 12 is the *anisotropic* ion diffusion coefficient (D_{II}), which accounts for

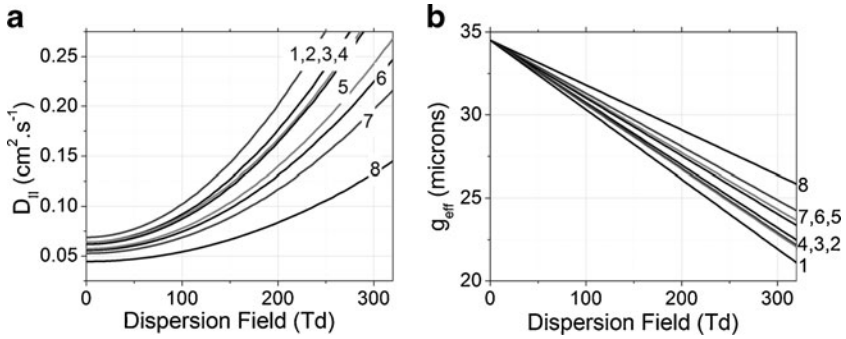

Fig. 13 **a** $D_{II}(E_D/N)$ for various product ions of differing K_0 (listed in Table 1) and **b** $g_{eff}(E_D/N)$ for the same ions. 1) dioxygen anion, 2) acetone monomer, 3) hydrated proton, 4) butanone monomer, 5) DMMP monomer, 6) acetone dimer, 7) butanone dimer, 8) DMMP dimer. All computations are at 318K (gas temperature) and 101.3 kPa with a 388 cm·min^{-1} gas flow rate and system configuration as per "Instrumental specifics"

longitudinal diffusional losses to the ion separator electrodes during transit [16]. D_{II} is defined by Eq. 14—

$$D_{II} = D\left[1 + \langle F_2 \rangle F_{II} M K_0^2 N_0^2 (E_D/N)^2/(3k_b T)\right] \quad (14)$$

where M is the molecular weight of the drift gas (kg), D is the isotropic diffusion coefficient defined by the *Einstein relationship*—

$$D = k_b T K_0 N_0 / qN \quad (15)$$

and F_{II} is a property of the ion–neutral molecule potential, which may be *approximated* by Eq. 16 (in which m is the molecular weight of the ion). The other terms appearing in Eqs. 13, 14 and 15 have their previous meanings.

$$F_{II} = 1 + (2m/(M + 2m)) \quad (16)$$

Replacing g_{eff} and D_{II} in Eq. 12 with an array of outputs from Eqs. 13 and 14, computed for a specific ion species, across the operational E_D/N range, we arrive at the purely *physical* field-dependent transmission behavior of the ion. This is exclusive of consideration of *intra-molecular* and *inter-molecular* ion–ion or ion–neutral interactions. In a theoretical analysis we do this for acetone, butanone and DMMP (monomers and dimers), as well as the hydrated proton and dioxygen anion (Fig. 14). What this reveals is the strong dependency on K_0, which should not be surprising given the appearance of the K_0 term in Eqs. 13, 14 and 15. The F_{II} contribution embedded in Eq. 14 is, by comparison, a negligible factor in determining the transmission behavior since, usually $m >> M$ and $2m/(M+2m)$ tends to unity (Table 1).

Higher field range (>120Td)

At higher E_D/N (>120Td) the above transmission model may begin to break down. The model does not account for (in particular); the kinetic and thermodynamic aspects of ion behavior within the ion separator, which are driven by the *field-heating* effect, where we define field heating as the raising of the *effective temperature* of the ion to a temperature exceeding its surroundings. Effective ion temperature scales ~$(E_D/N)^2$ so, as one enters the ultra-high-field operational regime, field heating strongly dictates the ion transmission behavior, since ions may dissociate, forming entities with entirely different K_0 values.

The field heating process is due to the conversion of kinetic energy acquired by ions in the applied field to thermal energy on collision with neutrals. In the absence of an applied field the total energy (E_T, J) of the ions and neutrals is defined by the Maxwell-Boltzmann relation; $E_T = \frac{3}{2} k_b T$. In an applied field the kinetic energy is raised by $\frac{1}{2} M v_D^2$ is the molecular weight average (kg) of the ions and neutrals (*which is effectively the average molecular mass of the neutral gas since the ion concentration relative to neutral carriers will always be very low*) and ν_D is the ion drift velocity at the discrete applied field. Referring back to "Field dependence of

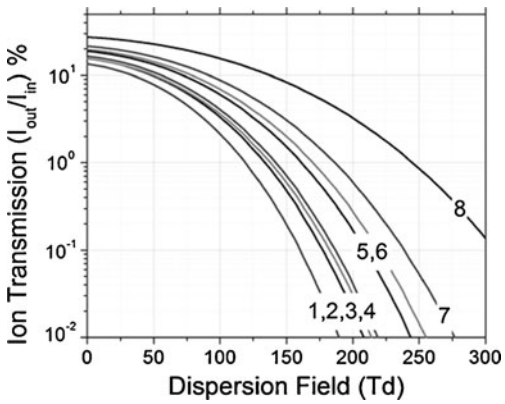

Fig. 14 **a** Ion transmission (without consideration of inter and intra-molecular interactions in the ion filter region) for various product ions of differing K_0 (listed in Table 1) at a gas temperature of 318K and pressure of 101.3 kPa. Numbering corresponds to ion identities shown in the caption to Fig. 13. All computations are at 318K (gas temperature) and 101.3 kPa with a 388 cm·min^{-1} gas flow rate and system configuration as per "Instrumental specifics"

Table 1 Molecular constants used in $D_{II}(E_D/N)$, $g_{eff}(E_D/N)$ and Ion transmission simulations (Figs. 18 and 19). Ion identity is speculated on the basis of a dry (<10ppm$_{(V)}$ H_2O) air drift gas. These K_0 values are carried over to experimental data evaluation in "Validation and discussion: observed vs. theory". K_0 reference sources are; *a* [36], *b* [37], *c* [38], *d* [39]

Case	Ion identity	K_0 ($cm^2 \cdot V \cdot s^{-1}$)	D ($cm^2 \cdot s^{-1} \times 10^{-2}$)	F_{II} *(No units)*
Hyd. O_2 anion	$O_2^-\cdot(H_2O)$	2.26 [*a*, *b*]	6.72	1.78
Acetone (M)	$(CH_3COCH_3)H^+\cdot(H_2O)_2$	2.11 [*a*, *c*]	6.24	1.87
Hyd. Proton	$H^+\cdot(H_2O)_2$	2.10 [*a*]	6.24	1.72
Butanone (M)	$(CH_3CH_2\ COCH_3)H^+\cdot(H_2O)_2$	2.03 [*a*, *c*]	6.03	1.88
DMMP (M)	$(CH_3)_2POOCH_3\cdot H^+\cdot(H_2O)_2$	1.88 [*d*]	5.59	1.92
Acetone (D)	$(CH_3COCH_3)_2H^+$	1.83 [*a*, *c*]	5.44	1.89
Butanone (D)	$(CH_3CH_2\ COCH_3)_2H^+$	1.73 [*a*, *c*]	5.14	1.91
DMMP (D)	$((CH_3)_2POOCH_3)_2\cdot H^+$	1.46 [*d*]	4.34	1.95

K" it can been seen $\nu_D = K_{(E/N)} E_D$ and the energy (E_T) can therefore be redefined by Eq. 17, where T is the ion temperature in the absence of the applied field and $K_{(E/N)}$ is the high field mobility ($m^2 \cdot V^{-1} \cdot s^{-1}$).

$$E_T = \frac{3}{2} k_b T + \frac{1}{2} M K_{(E/N)}{}^2 (E_D/N)^2 \quad (17)$$

If it is assumed that ion to neutral collisions are elastic and the kinetic energy acquired in the applied field is retained in the velocity of the ion (in a dynamic equilibrium with its surroundings) the ion temperature will be raised to an *effective temperature,* T_{eff} (K) and the total energy to $E_T = \frac{3}{2} k_b T_{eff}$. Insertion of $E_T = \frac{3}{2} k_b T_{eff}$ into Eq. 17 and factorizing terms, T_{eff} reduces to Eq. 18 whereby $K_{(E/N)}$ is replaced by $K_{(0)}$.

$$T_{eff} = T + M K_0^2 N_0^2 (E_D/N)^2/(3k_b) \quad (18)$$

Polyatomic molecular ion clusters, however do not undergo elastic collisions because some of the kinetic energy is conserved and distributed amongst the rotational and vibrational degrees of freedom of the molecular ion. T_{eff} will subsequently be reduced by a factor ζ, the *ion–neutral collision efficiency factor*[3]—

$$T_{eff} = T + \zeta M K_0^2 N_0^2 (E_D/N)^2/(3k_b) \quad (19)$$

For ion clusters of molecular weights representative of volatile and semi-volatile chemicals (100–400 $g \cdot mol^{-1}$) factors of ~0.4 to ~0.7 can be regarded as typical e.g., Krylov et al. [40] and applied fields of >80Td raise T_{eff} to many hundreds of Kelvin above the *neutral gas temperature* (T). This may promote dissociation and fragmentation of the ion, which may be considered by an analysis of kinetic processes on the ion within the ion separation region.

The residence time of an ion in the separation region is only a small fraction of that in the ionization region (which we define as the space between the ionizer and entrance to the ion separator). At very low $E_D/N < 10$ Td, where T_{eff} is only marginally higher than T, ions with a lifetime exceeding the residence time in the ionization region will remain intact on their traverse through the separation region. At increasing E_D/N however, ion reactions become kinetically favorable. Such processes may include; *1*) dissociation of *ion–dipole- (and ion-induced-dipole-)* bound solvating neutrals derived from the drift gas (e.g., H_2O, N_2, etc.), *2*) dissociation of proton bound species and *3*) dissociation via the cleavage of a covalent site (i.e., fragmentation). If E/N raises T_{eff} so as to favor ion dissociation by one or more of these processes (on the timescale of ion residence time integrated across all high field segments of the E_D/N waveform) the conformation of the ion on exit from the separator will not match that on its entrance and the transmission model described in "Lower field range (<150Td)" cannot hold (because K_0 changes with the conformation of the ion). Citing the above dissociation processes, one can generalize that the dissociation energies order; 1<2<3, since an ion–dipole interaction is weaker than an ionic hydrogen bond and a covalent bond is stronger than an ionic hydrogen bond. At increasingly high E_D/N (and hence increasing T_{eff}) these dissociation processes may be observed in the same order.

To set the scene in this discussion we shall model the dissociation of the symmetrical proton bound dimer (M_2H^+), to a protonated monomer (MH^+) and neutral (M), as defined by the general reaction—

$$M_2H^+ \rightarrow MH^+ + M \quad (20)$$

Under normal system operating conditions the concentration of M is << than other neutrals (the drift gas). The ion dissociates, as per Eq. 20, during the high-field portion of the waveform (when the ion is "hot"). However, the probability of the reverse *association* reaction is negligible during the low-

[3] The collisional efficiency factor (ζ) is also a function of the gas temperature (T). To simplify this initial analysis we assume it to be independent of T. In practice the gas temperature is fixed, eliminating this variable (i.e., such that it becomes wholly integrated within the empirically derived data).

field period of the waveform (when the ion is "cool") because the probability of a monomer (MH^+) and neutral (M) collision is negligible on the timescale of the low-field period. Under these conditions, the rate (r, mol·s^{-1}) of dissociation can be defined by the first-order rate law, where $[M_2H^+]$ is the concentration of dimer ions exiting the ion separator, t is the time the dimer ion spends in the ion separator (s) and k is the first-order rate constant (s^{-1}).

$$r = -d[M_2H^+]/dt = k[M_2H^+] \tag{21}$$

At time = t, the concentration of dimer ions in the ion separator $[M_2H^+]_t$, relative to the concentration of ions entering the separator at t=0 $[M_2H^+]_0$, can be expressed by the integrated first-order rate law—

$$[M_2H^+]_t = [M_2H^+]_0 \exp -kt \tag{22}$$

and the first-order rate constant (k) by—

$$k = -\ln[M_2H^+]_t/[M_2H^+]_0 \cdot 1/t \tag{23}$$

For the dimer cluster ion to make it through the separator and be detected its lifetime must exceed its residence time in the separator (t_{res}). Going a step further, for any dimer ions to be detected a finite proportion exceeding the level defining the signal to noise ratio of the system must remain undissociated on transit through the separation region. From Eq. 23, the half-life of the dissociation process ($t_{1/2}$) will be given by—

$$t_{1/2} = \ln 2/k \tag{24}$$

The dimer dissociation rate constant (k) will exhibit some dependency on the molecule from which the dimer originates. Positive ion mode dimers are bound by an ionic hydrogen bond and typical binding energies range 90–130 kJ·mol^{-1}, with dissociation rate constants <<1 s^{-1} at STP. This delivers stability at lower E_D/N, where T_{eff} is within a few tens of Kelvin of T (Fig. 20) and many dimers therefore present themselves through the lower half of the E_D/N scan range (<150 kV·cm^{-1}). However, k is extremely temperature dependent and at increasing E_D/N it may be expected that the ion residence time at high field ($D_{\tau(h)}$) (where the ion is "hot") tends to >>$t_{1/2}$, i.e. a vast proportion of dimer ions break down and the dimer response disappears.

To predict/interpret the breakdown field an understanding of the relationship of T_{eff} in relation to k is required. This is given by the *Arrhenius equation* (Eq. 25) in which R is the ideal gas constant (8.3145 J·mol·K^{-1}), E_A the activation energy of dissociation (J·mol^{-1}) and A the Arrhenius constant (s^{-1}).

$$k(T_{eff}) = A \cdot \exp -(E_A/R\,T_{eff}) \tag{25}$$

E_A is related to the standard enthalpy of formation (−$\Delta H°$, J·mol^{-1}), which is the binding energy of the ionic hydrogen bond holding the dimer together through the expression $\Delta H° = E_A + RT$, where T is standard temperature (293.15 K). For many proton-bound dimers reference tables exist for ΔH°, e.g., *National Institute of Standards web book* [41] and thus E_A is calculable. The Arrhenius constant (A, which is usually a very high power of e) can be more difficult to look-up and very often this is derived empirically). There are, however examples that can be pulled out from the literature e.g., [42]. As an approximation, log$A$=16.0 may be employed. In this present analysis the proton-bound dimer of DMMP is taken as an opportune case example, since its breakdown has also been experimentally analyzed through DMS / FAIMS by An et al. [43].

Log$A$ and E_A for the dissociation of the DMMP dimer are shown in Table 2. Substituting these values in Eq. 25 one observes (unsurprisingly) the dramatic *exponential* increase in dimer dissociation rate constant (k) over the T_{eff} range (~300–1200 K) that correlates to the scanable E_D /N range of ~0–300Td at 101 kPa (for this DMMP dimer case). At ~160 Td, $t_{1/2} \approx D_{\tau(h)}$ and at 180 Td, $D_{\tau(h)}$ exceeds $t_{1/2}$ by >10 (Fig. 15).

The correlation between the thermal dependence of k and the ion transmission spectrum of the dimer will now become clearer. The ratio of dimer ions exiting the ion separator $[M_2H^+]_t$, to those entering it $[M_2H^+]_0$, can be determined from Eq. 22, by replacing t with $D_{\tau(h)}$ and k with $k(T_{eff})$, where $k(T_{eff})$ is the dimer dissociation rate constant at the effective ion temperature in the high-field portion of the applied waveform (i.e., T_{eff} at E_D/N). This yields Eq. 26, which ultimately defines the kinetic contribution to the shape function of the dimer Ion Transmission Spectrum (ITS).

$$[M_2H^+]_t/[M_2H^+]_0 = \exp -k(T_{eff})\, D_{\tau(h)} \tag{26}$$

Thus, where the dimer is stable in the ion separator, i.e. $k(T_{eff})D_{\tau(h)} << t_{1/2}$, a stable dimer response will be observed through the stepping of E_D/N (if losses to the separation electrodes due to anisotropic diffusion defined by the D_{II} term in Eq. 12 are neglected). However, at some point E_D/N raises T_{eff} such that $k(T_{eff})D_{\tau(h)} \approx t_{1/2}$ and then readily such that $k(T_{eff})D_{\tau(h)} >> t_{1/2}$. With the exponential dependency of $[M_2H^+]/[M_2H^+]_0$ on $k(T_{eff})D_{\tau(h)}$ this drop off is dramatic (Fig. 16)

Table 2 Molecular constants used for dimer ion transmission models (Fig. 16). ζ values are very roughly estimated at 318K using data presented for the DMMP dimer by Krylov et al. [40]

Dimer cluster (M_2H^+)	Log$A$ (s^{-1})	E_A (KJ·mol^{-1})	ζ (unitless)
Acetone	16.0	123.7	0.7
Butanone	16.0	124.7	0.7
DMMP	15.6	127.0	0.7

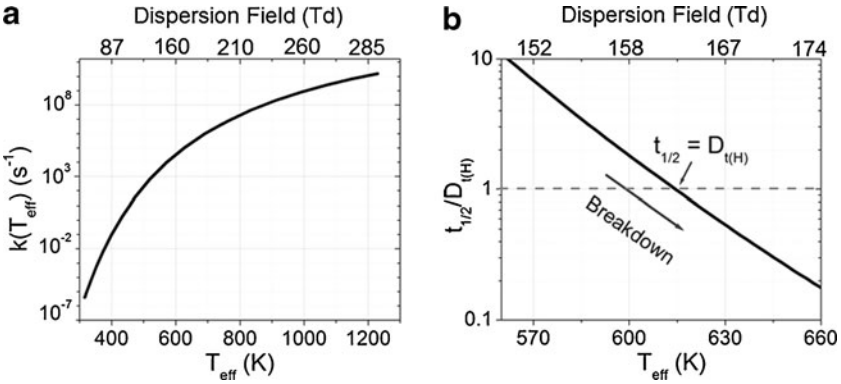

Fig. 15 **a** DMMP dimer dissociation rate constant (k) as a function of the effective ion temperature (T_{eff}) using LogA=15.6s^{-1} and E_A= 127kJ·mol^{-1} (with T_{eff} calculated from Eq. 19 using T=318K and ζ= 0.72). **b** Ratio of DMMP dimer half-life life to integrated high field drift period in the ion separator ($D_{\tau(h)}$) of 13.5 μs using $k(T_{eff})$ from **a**. The definition of the ion efficiency factor (ζ) is given in section 3.3.2

Peak width

For a planar FAIMS/DMS separator the peak width ($W_{1/2}$) as Full Width at Half Maximum (*FWHM*), V·m^{-1} is given by—

$$W_{1/2} = (4N/K_0N_0) \cdot (D_{II} \ln 2/t_{res})^{1/2} \quad (27)$$

where, t is the ion residence time (s) and the other terms have their previous meanings. D_{II} exhibits an E_D/N dependence by virtue of Eq. 14 and thus so does the peak width. At constant pressure the $W_{1/2}(E_D/N)$ function evolves from near flat at lower E_D/N (<100Td) to quadratic at very high E_D/N (>300Td) (Fig. 17). In the 0.5 mm planar FAIMS topology exploited by Krylov et al. [32] data was only gathered in the 0 to 120Td E_D/N range, meaning the effects of anisotropic diffusion on peak broadening were minimal (i.e., the peak width could be assumed relatively constant through their operational E_D/N range). For the very high E_D/N operation employed by the present authors this is not the case, as is clearly illustrated in Fig. 17 (which models the $W_{1/2}(E_D/N)$ responses for the example ion cases given in Table 1).

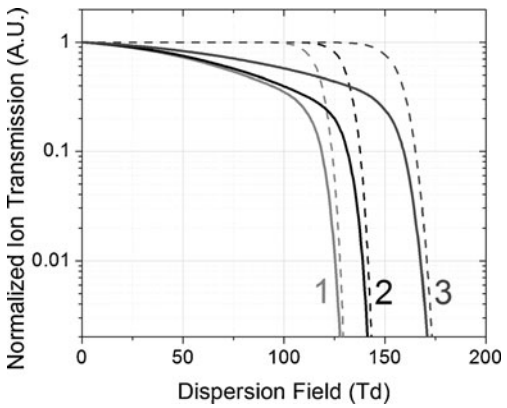

Fig. 16 *Dashed lines* (----) predicted proton-bound dimer ion transmission spectra at 101.3 kPa (where $[M_2H^+]_t/[M_2H^+]_0$ is assumed proportional to ion current, i.e., ignoring diffusional losses) for acetone (1), butanone (2) and DMMP (3) using log A and E_A and ζ constants for (T_{eff} calculation) shown in Table 2 and gas temperature (T) of 318K. *Solid bold lines* (—) are the same predicted transmission spectra where diffusional losses are also accounted. K_0 values listed in Table 1 were used in all computations

Validation and discussion: observed vs. theory

The model discussed in the previous section is somewhat semi-quantitative. Limitations include, for example, the estimates one makes relating the various molecular ion constants (e.g., ζ, k and A) and the approximation of K_E for K_0 in T_{eff} calculations. These limitations can be qualified in an experiment *vs*. theory evaluation and we do so in this section; examining the cases of acetone, butanone and DMMP cluster ions, as well as that of the positive and negative ion mode reactant ions (*which one assumes here to be the hydrated proton and hydrated dioxygen anion; of*

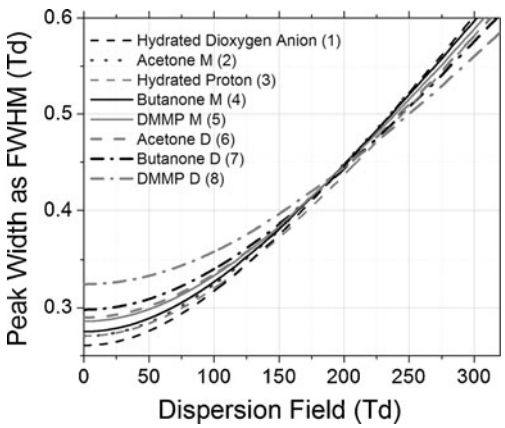

Fig. 17 Computed $W_{1/2}(E_D/N)$ curves for product ions of differing K_0 (Table 1). Numbering corresponds to the ion identities shown in the caption to Fig. 13. All computations are at 318K (gas temperature) and 101.3 kPa with a 388 cm·min^{-1} gas flow rate and system configuration as per "Instrumental specifics"

general formula $H^+(H_2O)_n$ *and* $O_2^-(H_2O)_n$). These cases have been chosen because they have been the subject of many IMS and DMS/FAIMS studies and many of the molecular ion constants defined in Eqs. 1 through 24 have been derived empirically. Acetone, butanone and DMMP also yield relatively stable monomer ion clusters, enabling assessment throughout our working E_D/N range, without the complication (in model evaluation) of ion fragmentation. In this particular evaluation and analytical treatment we draw specific attention to the work of the following; An et al. [43, 44], Krylov et al. [32, 35, 40], Eiceman and Stone [45], Ewing et al. [42] and Stone [46].

Experimental

Experimental conditions were set to replicate those employed by Krylov et al. [35]. Deviations from these conditions are explicitly highlighted.

Vapor sample preparations and system environmental parameters

Acetone, butanone and DMMP vapors were generated by PTFE incubated permeation sources. Vapor generation systems (OVG-4; *Owlstone Ltd., Cambridge, UK*) equipped with outlet spit flow controls were used for permeation source incubation and manipulation of vapor level output. The vapor generator diluent gas was clean dry air output from a *Zero Air* generator passed over a 90A molecular sieve and activated carbon filter. PTFE source permeation rates were determined gravimetrically over an incubation period of 4 weeks. Acetone, butanone and DMMP utilized in permeation sources was Analytical Standard grade, >99.9 % purity (*Sigma Aldrich, Poole, UK*). The split flow output of the vapor generator was mixed with a clean dry air flow of the same standard as that fed into the vapor generator, in order to manipulate the vapor level presented to the sensor platform. The gas flow rate through the sensor was 388 (±5) $cm^3 \cdot min^{-1}$. This consisted of a 18 $cm^3 \cdot min^{-1}$ sample inlet flow and 370 $cm^3 \cdot min^{-1}$ recirculating air flow. "At sensor" vapor levels studied ranged from 4 to 100 $ppb_{(V)}$.

Pressure was monitored continuously at the output of the sensor assembly (via the pressure sensor indicated in Fig. 6) and logged with the output ion current data for later Td conversion. Sample humidity was monitored at the sensor outlet by means of a high precision hygrometer (*Cermet II IS, Michell Instruments Ltd, Cambridge, UK*) and maintained <10 $ppm_{(V)}$ H_2O for all experimental data reported herein.

Spectral data acquisition and post processing

E_C.E_D spectra were generated with E_C drive settings of 401 data points in the −6 V to −6 V range and E_D settings of 51 points in the –0 to 60 V (V_b) range. This yielded 29.9 mV E_C resolution and E_D 1.1 V resolution respectively, equating to E_C/N resolution of ~40 mTd and E_D/N resolution of ~11 Td at 101 kPa). Spectra were obtained in replicates of at least 20 over the course of 10 days of experimentation. Raw spectra were processed off-line using a proprietary peak extraction algorithm, which reduced each raw spectrum to a set of Gaussian peak parameters (E_C/N, *Area* and *width*) at each E_D sample point in the scanned E_D/N range. Further post processing (mathematical/statistical processing and graphical representation) was performed using Origin version 6.0 (*Microcal Software Inc., Northampton, MA*).

Ion peak position

Krylov et al. [35] studied the field dependent mobilities of the gas-phase protonated monomers and proton-bound dimers of straight-chain ketones (of carbon numbers 3 to 10) in a dry air (~1 ppm H_2O) drift gas, using a planar FAIMS system configuration described by Miller et al. [4]. The α_2 and α_4 parameters (c.f. Eq. 5) for each ketone, under their experimental conditions, were determined with considerable precision (<5 % LSD). In a separate publication Krylov et al. [32] presented E_C:E_D spectra and alpha plots for the DMMP monomer and dimer, as well as the solvated proton and solvated dioxygen anion (respectively the positive and negative ion mode reactant ions). This information offered the present authors with an opportunity for comparison, utilizing the system described in "Instrumental specifics".

In Figs. 18 and 19 we compare empirically derived E_C:E_D responses, for the above mentioned cases, with the theoretical, utilizing α_2 and α_4 coefficients quoted (or derived) from the above mentioned literature. In spectral representation we transpose E_D/N (the independent variable in Eq. 9) to the Y axis and E_C/N (the dependent variable in Eq. 9) to the X axis, in convention with DMS / FAIMS standard for an intuitive spectral view (as illustrated in Fig. 10). The sign of the E_C/N axis is also reversed from that used in the above quoted literature to maintain convention with standard spatial representation of orthogonal axes. The *signs* of the α_2 and α_4 coefficients taken from the literature have therefore been reversed accordingly for this evaluation. Predicted responses have thus been modeled by means of Eq. 9, using the α_2 and α_4 coefficients shown in Table 3 and our known $<f_2>$, $<f_3>$ and $<f_5>$ waveform coefficients ("Instrumental specifics"). Our experimental data have been fitted to the *truncated* form of the alpha model using only data in the lower half of the working E_D/N range (<140 Td). Attempting to fit this truncated form of the model across the entire range leads to a poor fit since it predicts $E_C/N \rightarrow E_D/N$ at high E_D/N (c.f. "Ion peak position") and instead one needs to retain higher order terms (as also illustrated in Figs. 18 and 19). Comparison of

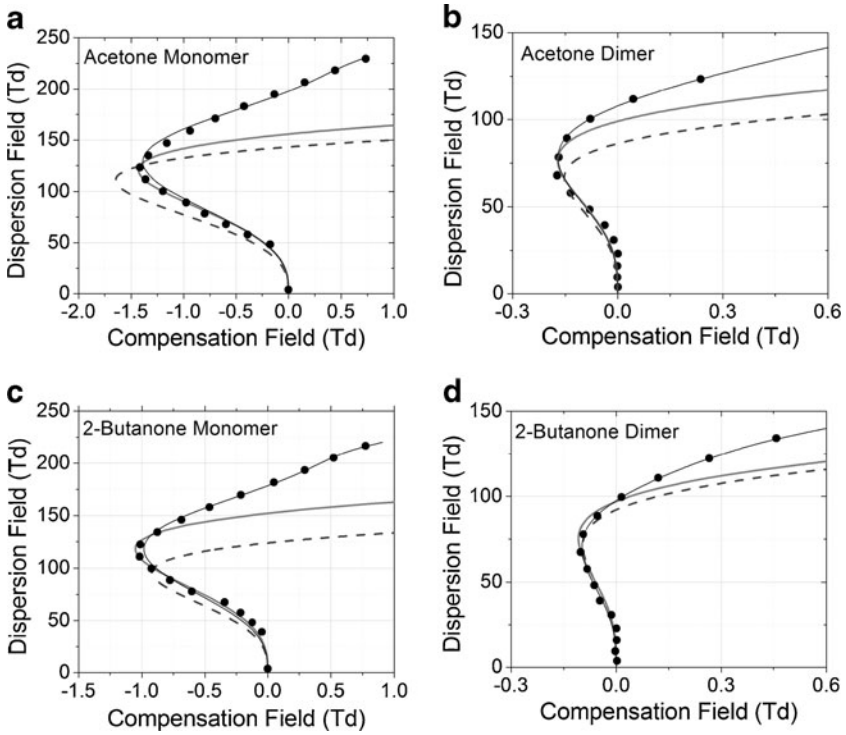

Fig. 18 Experimental (*black data points* •) and predicted E_C:E_D responses using the truncated form of the alpha-function (Eq. 9) with α_2 and α_4 inputs shown in Table 3 and waveform co-efficients determined in "Separation waveform analysis" (*dashed lines* ----) for acetone monomer (**a**), acetone dimer (**b**), butanone monomer (**c**) and butanone dimer (**d**). The *light grey lines* (—) are least squares fits of Eq. 9 to the low field (E_D/N <140Td) data points only, whilst the *black solid lines* are fit of an expanded form of Eq. 9 (Expanded to the ninth order, i.e., $E_c/N=c_3\cdot(E_D/N)^3+ c_5\cdot(E_D/N)^5+ c_7\cdot(E_D/N)^7+ c_9\cdot(E_D/N)^9$, in which the constants c_7 and c_9 are composed of the higher order α_n terms and higher order waveform co-efficients $\langle f_n \rangle$). Experimental uncertainties in the determined E_C/N values are less than the range captured within the area of the plotted data points (i.e., <0.05Td)

experimentally derived α_2 and α_4 coefficients at lower E_D/N with those published, nevertheless makes a useful point of reference in discussion. These derived α_2 and α_4 coefficients are also shown in Table 3.

On first inspection Table 3 may seem alarming because of the marginal correlation between the comparative sets of α_2 and α_4 coefficients (a marginal correlation that is illustrated explicitly in Figs. 18 and 19). However, it must be appreciated that the α parameters are very dependent on experimental conditions, in particular the ppm_v water concentration at the sensor (particularly at significantly sub-ambient moisture levels, <10 $ppm_{(v)}$). "Experimental" indicates that we were only able to roughly replicate the experimental conditions described in the literature. It is the qualitative comparison that is of more interest and *critically* one must remember that chemical classification is based only partially on the E_c;E_D profile in ion separations performed at ultra-high-fields (as shall be discussed in "Ion peak intensity & ion transmission" and "Ion peak width").

Acetone and butanone

Qualitatively, the monomer and dimer responses of both acetone and butanone (comparing experimental data with the predicted responses) agree well at lower E_D/N range. For the monomers the alpha model fits well at E_D/N <140 Td and for the dimers it fits well at E_D/N <100 Td. At higher E_D/N the alpha model breaks down for both monomer and dimer as theorized. The monomer response extends to a considerably higher E_D/N than the dimer. The dimer response would be expected to decay in the mid E_D/N range because of field-induced dissociation at the higher effective ion temperatures encountered in this mid E_D/N range. This shall be discussed further in "Ion peak intensity & ion transmission".

With respect to the deviation of the monomer response from the alpha model at higher E_D/N it may be accurately stated that at higher E_D/N the effective ion temperature in the lower-field period of the applied waveform actually becomes appreciably higher than the gas temperature and that the approximation of the ion mobility to K_0 made in Eq. 5 is no longer valid. For example, at a peak field of 200 Td the maximum field in the low-field period reaches ~70 Td. It may further be postulated that the model focuses too heavily on the physical process of the "solvation and desolvation" of neutrals. Whilst this is effective in the lower half of the E_D/N range (where effective ion temperatures are modulated only to within a few hundred K of the gas temperature) it may not be expected to be as effective at

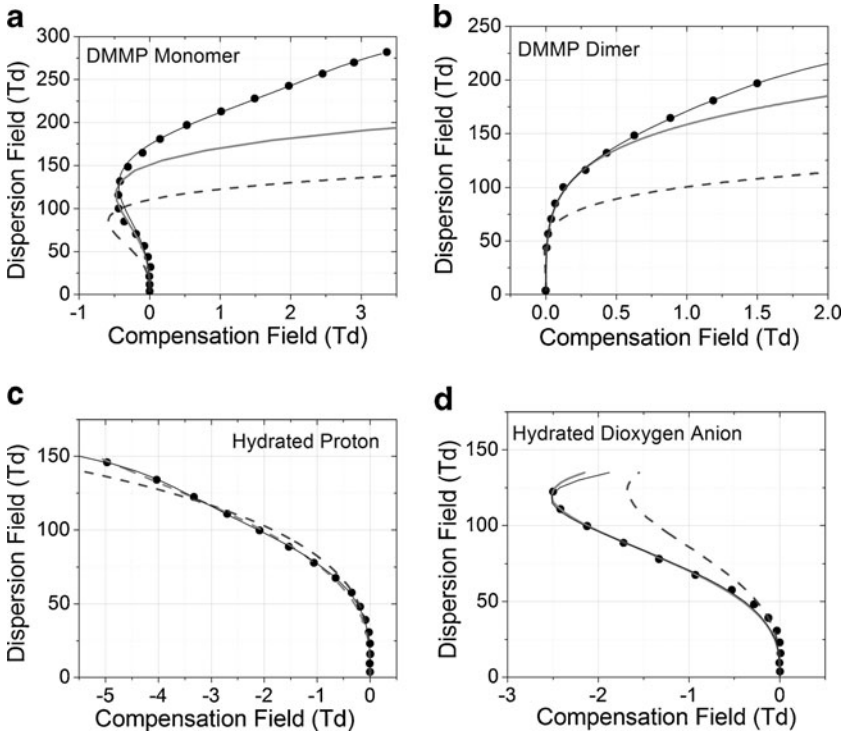

Fig. 19 Experimental (*black data points* •) and predicted E_C:E_D responses using the truncated form of the alpha-function (Eq. 9) with α_2 and α_4 inputs shown in Table 3 and waveform co-efficient determined in "Separation waveform analysis" (*dashed lines* ----) for; DMMP monomer (**a**), DMMP dimer (**b**), hydrated proton (**c**) and dioxygen anion (**d**). The *light grey solid lines* (—) are least squares fits of Eq. 9 to the low field (E_D/N <140Td) data points only, whilst the black solid lines are fit of an expanded form of Eq. 9 (see Fig. 18 Legend). Experimental uncertainties in the determined E_C/N values are less than the range captured within the area of the plotted data points (i.e., <0.05Td)

higher E_D/N, where effective ion temperatures become so high that that the ion cluster is entirely desolvated. This is discussed further in "Ion peak intensity & ion transmission", since the ion transmission spectrum provides additional information for this debate.

DMMP

The monomer and dimer responses of DMMP (Fig. 19a and b) do not fit as well with the Krylov et al. [32] predicted responses, although the alpha model still holds in the lower half of the E_D/N scan range. There was some uncertainty with respect to the precise experimental conditions employed by Krylov et al. [35] (e.g., $ppm_{(v)}$ H_2O and gas temperature) and any mismatch in conditions employed in this present work and the conditions employed in the work of those authors would invalidate any comparison. Instead we focus on a comparison with our own acetone and butanone responses (shown in Fig. 18). The gross observation for both the monomer and dimer cases are the much reduced

Table 3 α_2 and α_4 coefficients determined by Krylov compared with those obtained in this work

Case	Literature [32, 35]		This work	
	α_2	α_4	α_2	α_4
Acetone (M)	-3.1×10^{-5}	9.5×10^{-10}	-2.1×10^{-5}	1.2×10^{-9}
Acetone (D)	-1.3×10^{-5}	1.8×10^{-9}	-9.9×10^{-6}	1.1×10^{-9}
Butanone (M)	-2.7×10^{-5}	1.2×10^{-9}	-1.7×10^{-5}	9.7×10^{-10}
Butanone (D)	-8.0×10^{-6}	6.0×10^{-10}	-6.6×10^{-6}	7.9×10^{-10}
DMMP (M) [a]	-2.5×10^{-5}	2.5×10^{-9}	-7.7×10^{-6}	4.1×10^{-10}
DMMP (D) [a]	-3.8×10^{-6}	1.5×10^{-9}	7.2×10^{-7}	8.0×10^{-11}
Hyd. Proton [a]	-1.7×10^{-5}	2.6×10^{-11}	-2.5×10^{-5}	9.0×10^{-10}
Hyd. O_2 anion [a]	-2.3×10^{-5}	1.3×10^{-9}	-3.8×10^{-5}	2.7×10^{-9}

[a]These literature values were derived from data presented in Fig. 3 of Krylov et al. [32], whilst the others were taken directly from Table 1 of Krylov et al. [35]

$-E_C/N$ of the turning point and extension of each response to a higher E_D/N. This is interpret in terms of the relatively larger collision cross sections (Ω) of the monomer and dimer of DMMP (compared to their acetone/butanone counterparts), which is reflected in their lower respective ion mobilities (Table 1). Solvation/desolvation with neutrals thereby contributes less to the ΔK between high and low field, reducing the negative E_C/N shift.

Reactant ions

The reactant ions present in the lower half of the E_D/N scan range only. Transmission losses may be expected to attenuate the reactant ion signals at high fields because of their relatively high mobilities (c.f. Table 1 and the D_{II} term in Eq. 12). The positive ion mode reactant ion (which we assume here to be the hydrated proton) correlates very well with that predicted through the literature comparison, whereas the correlation with the negative ion mode reactant ion (which we assume to be the hydrated dioxygen ion) shows some deviation. The latter is tentatively considered to be an artifact of the use of a corona ionization source by the present authors (as opposed to a Ni^{63} ion source used in the literature quoted system). This hypothesis is evaluated further by consideration of the ion transmission and peak width data ("Ion peak intensity & ion transmission" and "Ion peak width").

Ion peak intensity & ion transmission

The *Ion Transmission Spectrum* (ITS), which the authors define as the integrated ion current of a resolved (or partially resolved) peak (as a function of E_D/N) is equally, if not more important, for classification purposes in ultra-high-field operation. Specifically the ITS is able to reveal information relating ion kinetics within the ion separator.

Reactant ions

The positive ion mode and negative ion mode reactant ions (for which data was generated simultaneously) make for an attractive study case, since in a clean system they present themselves wholly independently. The transmission spectra relating to Fig. 19c and normalized to the ion transmission at $E_D/N = 0$ are shown in Fig. 20. The ion transmission can be approximated to Eq. 12 (with normalization eliminating pre-exponential factors), whereby the key parameter becomes K_0 embedded in the D_{II} and g_{eff} terms. The positive ion mode reactant ion seems to be the more straightforward of the two cases to explain. The transmission profile fits between that predicted for the $H^+(H_2O)_n$ of K_0=2.10 and 2.45. At increasing E_D/N the solvation number (n) of the cluster is expected to reduce and with this the ion mobility (K) increases. The transmission profile transits from that for the cluster with the higher n (lower K) to that with lower n (higher K).

The Negative Ion Mode response is less obvious. Under the experimental conditions the reactant ion would be expected to be either mono-hydrated $[O_2^-(H_2O)]$ or de-hydrated $[O_2^-]$, given the observations by Krylov et al. [40] in their evaluation of Temperature Effects in FAIMS. However, neither K_0 fits the observed profile. A non-linear least-squares fit of Eq. 12 to the data extracts a K_0 of 2.70 (±0.03) $cm^2 \cdot V^{-1} \cdot s^{-1}$, which suggests a different negative reactant ion (possibly derived from the corona ion source). A mass-spectral evaluation of corona ion chemistry has subsequently been undertaken and will be a subject of a separate article.

Dimers

A model for the dimer response was well established in "Ion peak intensity", where it was shown that the precise breakdown field of a dimer will be dictated by the effective-ion-

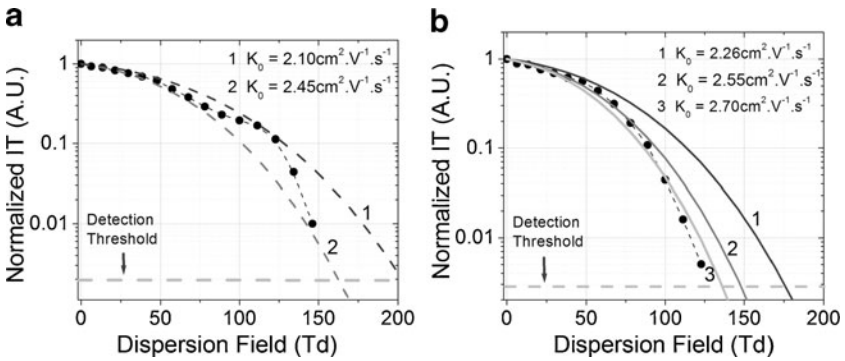

Fig. 20 **a** Positive ion mode reactant ion transmission spectra. Experimental data (normalized to the integrated peak ion current at E_D/N=0) is indicated by *black circles* (•) with *dashed line* (----) beta spline connectors. *Dashed line* **1** is the predicted ion transmission using a K_0 of 2.1 $cm^2 \cdot V \cdot s^{-1}$ and *dashed line* **2** is that using a K_0 of 2.45 $cm^2 \cdot V \cdot s^{-1}$. **a** Negative ion mode reactant ion transmission spectra. Experimental data (normalized to the integrated peak ion current at E_D/N=0) is indicated by *black circles* (•) with *dashed line* (----) beta spline connectors. *Solid line* (—) **1** is the predicted ion transmission using a K_0 of 2.26 $cm^2 \cdot V \cdot s^{-1}$ and *dashed line* **2** is that using a K_0 of 2.55 $cm^2 \cdot V \cdot s^{-1}$. *Solid line* **3** is a non-linear least-squares fit of Eq. 12 to the experimental data

temperature-dependent first-order rate constant $k(T_{eff})$ and the integrated high-field ion residence time of the ion in the separation channel ($D_{\tau(h)}$) (c.f. Eq. 26). The experimental ITS for each of the three study cases (Acetone, Butanone and DMMP) are shown in Fig. 21, with the predicted responses (combining diffusional and kinetic transmission losses) overlaid. Field-dependent dimer breakdown is evident in the experimental data. The correlation between the experimental and predicted transmission spectra is not exact but this must be expected because of model approximations. We summarize that the breakdown for butanone and acetone occurs at a lower than predicted E_D/N. This suggests that the ion-neutral collisional efficiency factor (ζ) of 0.7 (used in the $T_{eff}(E_D/N)$ computations input into the transmission model) was overestimated, assuming confidence in the K_0 parameters listed in Table 1 and the Log$A$ and E_A parameters listed in Table 2. For DMMP we observe that the breakdown occurs at an E_D/N of the order expected when using ζ=0.55 in the $T_{eff}(E_D/N)$ computations input into the transmission model. This is the ζ value estimated at the gas temperature (318K) using $\zeta(T)$ data from An et al. [43]. On the other hand, using ζ=0.7, estimated from the $\zeta(T)$ data of Krylov et al. [40], yields a poorer correlation between experiment and model.

Whilst dimer breakdown is the prominent feature in the dimer ITS, transmission behaviors at E_D/N below the breakdown threshold should not be neglected. Below 100Td kinetic losses are negligible and the transmission is dictated wholly by Eq. 12. Experimental observations in this lower E_DN region deviate from the predicted and there are subtle features ("dips", etc.) embedded in the transmission profile at lower E_D/N that

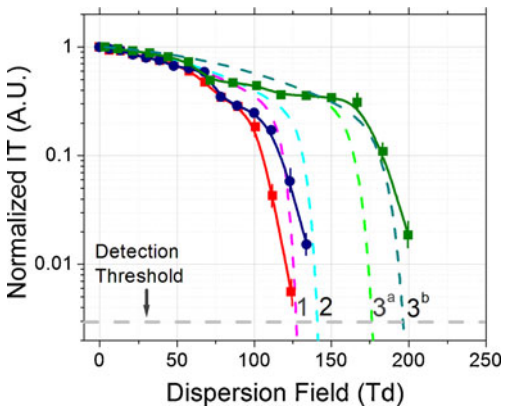

Fig. 21 Normalized Ion transmission spectra at gas temperature 318K for acetone (*red squares* ■), butanone (*blue circles* ●) and DMMP (green squares ■) dimers, where error bars are 1 standard deviation of the mean. Predicted responses for acetone (1) butanone (2) and DMMP (3_a and 3_b) are indicated with *dashed lines* (----). The predicted responses are based on the combination of field dependent diffusional losses and kinetic losses determined by Eqs. 12 and 26, using input data shown in Tables 1 and 2. For DMMP 3_a has been determined by using ζ=0.7 [40] in the $T_{eff}(E_D/N)$ computations input into the transmission model, whereas 3_b uses ζ=0.55 [43]

suggest higher order ion transport phenomena. Again, the experimental data are too sparse to comfortably qualify this discrepancy. However one may postulate that K_0 uncertainties in the $D_{II}(E_D/N)$ computation are a contributory factor. A higher resolution study of the ITS would be beneficial to evaluate this.

Monomers

Acetone, butanone and DMMP monomers are thermally stable; that is they are not prone to fragmentation at an intramolecular (covalent) site, except at very high T_{eff} (~900 K). They are also relatively small molecules, so when thermally induced fragmentation does occur, the fragmentation products will be of low MW (and of small collision cross-section). They will have a mobility greater than that of the parent ion. On this basis one may presuppose that when the presence of dimer is suppressed (by keeping the vapor concentration at the sensor low) an ITS that strictly follows Eq. 12 (and similar to reactant ions, shown in Fig. 20) would be observed (*since at fragmentation any fragment ions will exhibit diffusional transmission losses that exceed the ion detection threshold*). This hypothesis was tested by observing the ion transmission spectra of Acetone, Butanone and DMMP at sensor levels of 4 $ppb_{(v)}$—a vapor level that was found sufficiently low so as to reduce the dimer response to <1/5th that of the monomer response at the monomer/dimer peak resolution point (~40 Td). The results are shown in Fig. 22.

Whilst there is some correlation between the observed and predicted ITS at lower E/N, there is an explicit lack of correlation at higher E/N. Equation 12 predicts the transmission to decay exponentially with increasing E/N whereas the profile "valleys" (point *i*), "peaks" (point *ii*) and then "decays" (point *iii*) below the peak detection threshold on scanning through the 120–250 Td range. At point B, the observed transmission exceeds the predicted by a factor >10^2. Whilst this observation is surprising and we are as yet unsure as to the precise physical process responsible for this effect[4], it is ultimately beneficial. First, it delivers much improved sensitivity in the mid E_D/N scan range and secondly the valley (*i*) and peak (*ii*) points (as well as well as the end point *iii*) exhibit molecular selectivity. In respect of the latter, the monomer ITS delivers a useful classification feature.

At higher vapor concentrations, where the dimer to monomer peak ratio is >> 1 (in the lower E_D/N range) an ITS response of the form shown in Fig. 22 may appear more

[4] It has now been considered that the reduced ion residence time of newly formed monomer ions in the separation region (generated on dimer breakdown) will lead to some additional increase in monomer response (since these ions have less of the ion separator to travel through and are less susceptible to diffusional losses). However, at the time of writing a full numerical analysis of this hypothesis was incomplete.

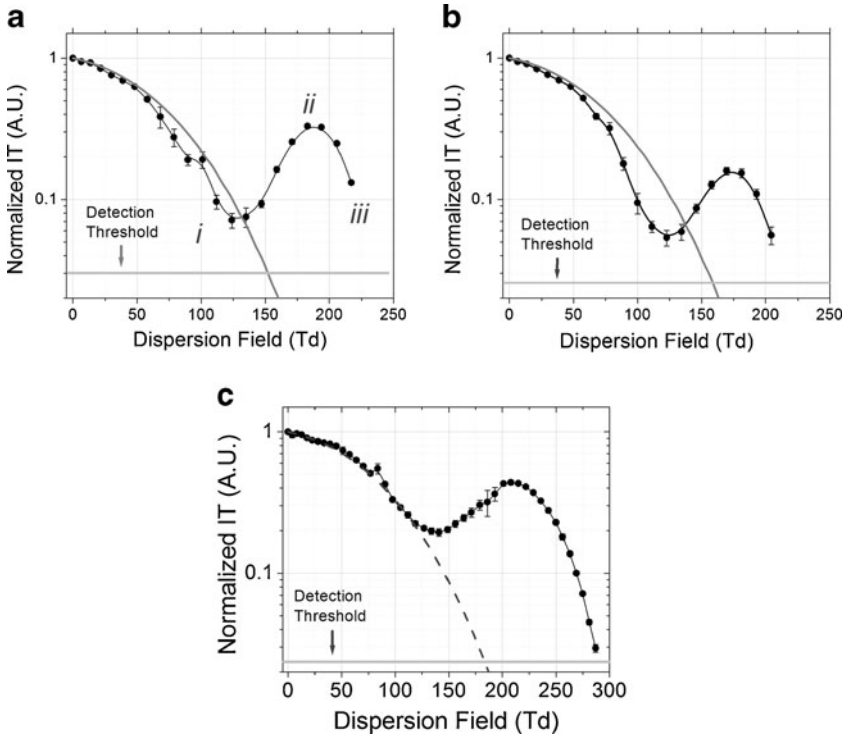

Fig. 22 Observed monomer transmission spectra for **a**) Acetone, **b**) butanone and **c**) DMMP (data points • with beta spline interpolation connectors —) compared with theoretical responses (*grey solid/dashed lines*)

rational. At lower E_D/N the dimer will be dominant and the monomer suppressed. However, at mid E_D/N the dimer will break down and Eq. 22 predicts this will result in an increase in monomer concentration within the ion separator. "Resurgence" in the monomer response would thereby be expected. We can model this hypothesis and compare it with empirical data. Below the dimer breakdown point we can denote the dimer concentration relative to the monomer concentration as $b.[M_2H^+]$ and that of the monomer $d.[MH^+]$, where b and d are the E_D/N diffusion dependent transmission factors predicted by the exponent part of Eq. 12. As the dimer breaks down the monomer concentration in the ion separator will become defined by—

$$[MH^+] = d[MH^+] + (d[MH^+] \cdot (1/bx \cdot [M_2H^+])) \qquad (28)$$

where x is the fraction of dimer at $T_{eff}(E_D/N)$ predicted by Eq. 26. Qualitatively Eq. 28 predicts that the monomer ion transmission response will initially decay in the lower E_D/N range (according to Eq. 12) until dimer breakdown starts occurring in the mid E_D/N range, whence it will rise again (since new monomer ions are formed within the ion separator). The response will then peak (once the dimer breakdown is effectively complete) before decaying again, from the peak point, in accordance with Eq. 12.

In Fig. 23 we assess this model against experimental data for acetone at a vapor concentration of 80 (±10) $ppb_{(v)}$ (whereby the dimer peak intensity at low E_D/N was observed to exceed the monomer by ~8:1). As expected the experimental data reveals a strong resurgence in monomer ion transmission (due to monomer formation in the ion separator as the dimer breaks down). However, the response does not properly correlate with that modeled by Eq. 28. Instead, the monomer transmission response shows a shift to higher E_D/N (i.e., an improved transmission function) and the monomer peak response exceeds that predicted by a factor of ~2. These observations highlight deviations at high E_D/N from conventional ion models and further investigation is required in order to derive a physical explanation. This will be the subject of a future publication. For now, one may derive some content with the conclusion that monomer ion transmission is more

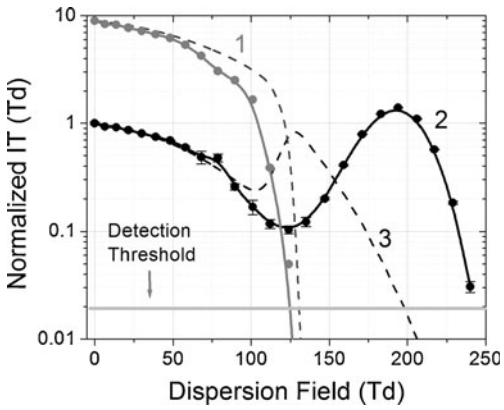

Fig. 23 Observed and predicted ITS for the acetone monomer (1) and dimer (2) at 80$ppb_{(V)}$ vapor concentration. Data has been normalized to the extrapolated monomer response at E_D/N=0. *Black circles* (•) with beta spline interpolation connectors (—) are experimental data while *dashed lines* are the predicted responses (see text)

efficient than that predicted by Eq. 12, ultimately resulting in improved sensitivity through the higher end of the E_D/N range.

Ion peak width

Replacing D_{II} in Eq. 27 with *the Einstein Equation* (Eq. 15) it is possible to derive an expression that allows for the determination of K_0 from the peak width ($W_{1/2}$, V·m^{-1}) at zero E_D/N—

$$K_0 = \frac{16N \ln 2 \cdot k_b T}{N_0 \, q t_{res} \, W_{1/2}^2} \tag{29}$$

On initial inspection this appears an attractive means by which to determine K_0 from the empirically derived $W_{1/2}$. However, there are two complications. First, there is of course no ion separation at zero field, so for species generating more than one ion, the zero field peak is a sum of the individual Gaussians. Secondly, the ion residence time must be accurately defined, which as we have seen in "Definition of ion residence time" is challenging since the flow velocity in the ion channel can only realistically be approximated to within a few percent in a rectangular micro-channel. It is possible nonetheless, to focus on a clean dry air sample and compare observed peaks for the hydrated proton and hydrated dioxygen anion with the theoretical prediction. One may go a step further and accurately establish the true ion residence time by substituting well referenced K_0 values for these particular "air derived" reactant ions.

Reactant ions

We begin by looking at the experimental vs. predicted $W_{1/2}(E_D/N)$ responses for the reactant ions (Fig. 24). At low E_D/N (<50 Td) a good correlation between experiment and theory is observed (when substituting the K_0 values shown in Table 1 into the Eq. 27). Just a small, relatively constant offset of 0.02 Td between experiment and theory is observed. If it is assumed that the ion residence time (t_{res}) is accurately defined, one might suggest that this is due to a discrepancy between the actual K_0 and that input in the model for $W_{1/2}$ determination and it is possible to test this.

Extrapolating the observed $W_{1/2}(E_D/N)$ data points in the 0–50Td range to zero (Fig. 24b), one obtains a zero Td $W_{1/2}$'s of 0.2738 (±0.0013) for the hydrated dioxygen anion and 0.2883 (±0.0010) for the hydrated proton. Feeding these values into Eq. 29 yields a K_0 of 1.99 (±0.01) cm^2·V·s^{-1} and 1.80 (±0.01) cm^2·V·s^{-1} for the respective cases (compared to their literature values of 2.26 and 2.10 cm^2·V·s^{-1}). One would conclude from this (assuming our reactant ion identities are correctly assigned) that t_{res} is not acutely defined. If the reverse problem is solved and the literature quoted K_0 values are used in combination with the zero Td extrapolated experimental $W_{1/2}(E_D/N)$ data, in order to obtain t_{res}, one obtains t_{res}=31.9 (±0.2) μs for the hydrated dioxygen anion and 30.9 μs (±0.2) for the hydrated proton. This compares to a computed t_{res} at the working flow rate (388 cm^{-3}·min^{-1}) of 36.9 μs. It may seem that a further analysis of the micro-channel gas flow is warranted. However, it must not be neglected that the ion transmission spectra (Fig. 20) would not correlate as well under the assumption of a shorter t_{res} (since ion transmission would increase). It seems more likely that there is an additional factor that broadens the peak.

Moving on to consider the $W_{1/2}(E_D/N)$ response at higher E_D/N one observes a considerable deviation from experiment and theory. $W_{1/2}(E_D/N)$ does not evolve smoothly and begins to exceed the predicted $W_{1/2}$ appreciably (> twice the predicted $W_{1/2}$ at ~110 Td). The additional broadening may be attributed to one or a combination of 3 factors. First, we may be running into a situation whereby we encounter an assembly of ions of differing hydration number—$(H_2O)_n$. The reactant ions are very small and have high K values >2.1 cm^2·V^{-1}s^{-1}. Any change in hydration number will have a large impact on K and the ion assembly will become "partially" resolved into its $\Delta K(E_D/N)$ elements. However, the resolution is not sufficient for the peak extraction algorithm to pick out the peaks and they become integrated as a single broad peak. The second aspect is that at increasing field the ion is driven toward desolvation (dissociation of the ion–dipole bound water neutral). Near the dissociation point

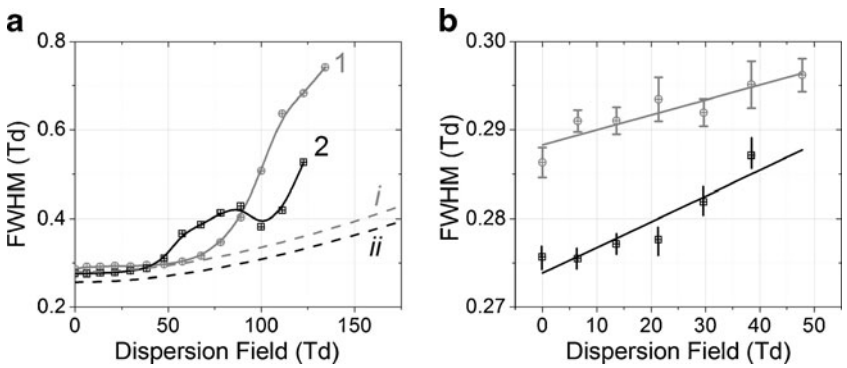

Fig. 24 **a** Observed (1 and 2) and predicted (i ad ii) $W_{1/2}(E_D/N)$ profiles for the positive ion mode and negative ion mode reactant ions (of assumed identity given in Table 2). **b** Experimental positive ion mode (1) and negative ion mode (2) observed in the 0–50Td range, where the error bars are standard deviations (n=20)

the collision cross-section of the ion increases disproportionally (particularly for small cluster ions) and K undergoes a rapid decrease over a narrow E_D/N range. This broadens the peak by virtue of Eq. 27. The third aspect, relating also desolvation, is that at increasing E_D/N the equilibrium of cluster ion species in the separator shifts from higher solvation number (lower K) to lower solvation number (higher K). Newly created ions within the ion separator have a shorter separation path (i.e., shorter t_{res}), which leads to a broadening of the peak by virtue of Eq. 27.

Monomers and dimers

Whilst, for the monomers and dimers presented in this case study it is not possible to effectively evaluate the $W_{1/2}(E/N)$ response at very low E_D/N (<50 Td) due to marginal peak resolution, it is informative to study the response at higher E_D/N where the peaks are fully resolved. The observed and predicted responses for the monomers/dimers are shown in Fig. 25. At lower E_D/N (<130 Td) experimental and predicted data do correlate well. At higher E_D/N an increasing deviation from the predicted is observed. In the case of the dimer the observed $W_{1/2}(E_D/N)$ tends *exponential* around the breakdown field. The monomer response is more stable but shows unusual features (turning points similar to those observed for the hydrated dioxygen anion). They may be related to the K variations invoked through field induced desolvation. Ultimately a higher-resolution study is required to fulfill understanding here. However, it should be appreciated that these turning points may be expected to be ion-specific and may therefore of use in analyte classification.

Conclusions

This paper has drawn attention to differences in the operational models applied in conventional lower field range DMS/FAIMS systems as compared to a system that operates over a significantly higher field range. The system described has been evaluated over a field range of 0–300 Td, approximately *doubling* the field range explored in previously described systems (e.g. those based on designs first presented by Guevremont and Purves [3] and Miller [4]). The key aspect of higher-field operation is the non-linear dependency of effective ion temperature on applied electric field. Doubling the operational field significantly increases the effective temperature range over which an ion can be studied because of the $\sim T_{eff} \propto (E_D/N)^2$ dependency. For smaller volatile and semi-volatile molecules (<300 AMU) T_{eff} >1000K may be reached. This has profound outcomes, since the high effective ion temperatures lead to the fragmentation of ions within the ion separation region and these fragmentations can be expected to exhibit field-dependent specificity by virtue of their unique kinetic and thermodynamic constants. Existing FAIMS/DMS models presented by Guevremont [5] and Krylov et al. [32] have been evaluated but do not necessarily represent ion separations fully at higher operational fields. In particular, the truncation of the α-function to the fourth order (α_2 and α_4 terms only), does not hold up well above ~150Td, even for stable ions that do not readily dissociate. For more stable ions, such as the acetone, butanone and DMMP examples used in the case study of this communication, higher order α terms become important. Nonetheless, these operational models have been invaluable in the system characterization presented herein and it is hoped that the paper may serve, in part, as a useful review of these models.

It must not be neglected that higher effective fields may also be generated in systems with limited waveform voltage range by reducing the operational pressure. High ion temperatures may then, in principle, be exploited in these systems too. For example, at 0.5atm (~50 kPa) a system delivering a high-field range of 0 to 150 kV·cm^{-1} will establish an effective field range of 0–300 Td. However, a

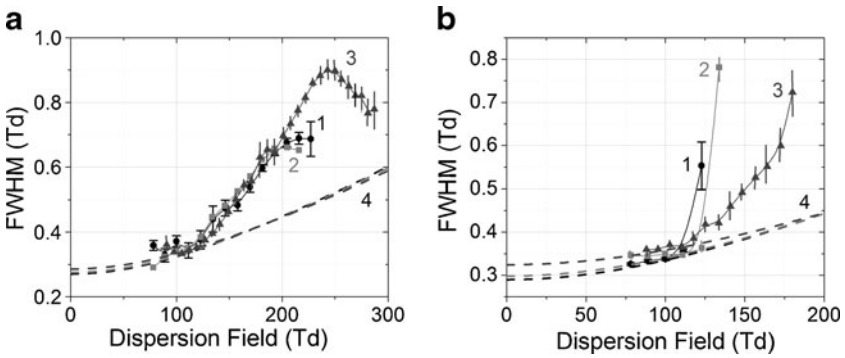

Fig. 25 **a** Experimental $W_{1/2}(E/N)$ responses for acetone (1), butanone (2) and DMMP (3) monomers shown as data circles (•), squares (■), and triangles (▲) respectively (with beta spline interpolation) compared with predictions (4) shown as *black dashed lines* ---- (acetone), *light grey dashed lines* ----- (butanone) and *dark grey dashed lines* ----- (DMMP). **b** Dimer responses (with equivalent annotations). Errors are standard deviations, where for acetone and butanone n= 20, whilst for DMMP n=5)

challenge associated with low pressure operation is the loss of ion transmission (and thus sensitivity), particularly at lower operational waveform frequencies, since ion transmission is $\sim \propto 1/(E_D/N)^2$. Further, the width of a (stable) ion peak is $\sim \propto 1/P^{1/2}$ (at fixed ion residence time), so a reduction in operational pressure has a resolution penalty, without any increase in the ion separation time and thus data rate. In summary, the authors have elected to operate with a short ion channel, fast separation, high ion transmission topology in combination with ultra-high field drivers, in order to exploit the analytical information available at ultra-high-fields. Whilst a subject for further debate, the Ion Transmission Spectrum (ITS) offers much potential for improved high data rate classification when used in conjunction with the conventional E_C:E_D spectral response.

It should be pointed out that in laboratory based operational scenarios, systems operating over lower operational field ranges may be optimized for separation performance though the addition of neutral modifiers to the make-up gas flow (e.g. [23]). The separation characteristics are optimized through the neutral species influence on ion cluster chemistry. However, this paper has focused rather more on the means of the exploitation possibilities of a stand-alone and rapidly fieldable sensor platform, by accessing analytical space at ultra-high fields. This paper has presented a platform with such a stand-alone potential; that is a packaged miniature spectrometer has been developed measuring 12× 12×15 cm, weighing 1.2 kg and consisting of the core multi-micron gap ion separator assembly and RF/DC electronic drivers integrated with pneumatic handling/sample conditioning elements, together with ancillary temperature, flow and humidity sensing for stable closed loop operation under local microprocessor control.

It is appreciated that *ab inito* spectral modeling at ultra-high fields is complicated by uncertainties in molecular ion constants, in particular the ion–neutral collision efficiency factor (ζ) and kinetic parameters that dictate fragmentation (i.e., the Arrhenius constant A and the effective-ion-temperature-dependent rate constant $k(T_{eff})$. In practice, empirical training delivers data in which these constants are wholly integrated and critically, a mature, well-characterized system solution has been described that can allow these training data to be generated with confidence. Comprehensive system evaluation remains to be communicated. In particular it is now necessary to define key system metrics (sensitivity, resolving power, chemical selectivity and quantitative response) in the context of real world analytical applications. Attention need also be paid to chemometric methods applied to real time data handling. The system is currently undergoing extensive laboratory and field trials in relation to trace Volatile Organic Compound (VOC) and Toxic Industrial Chemical (TIC) monitoring. The data output from this activity will enable full attention to be paid to system metrics and chemometric methods. It is envisaged that this present communication will serve as a clear reference point for these forthcoming application specific technology evaluations.

Acknowledgements The financial support from the US Defense Threat Reduction Agency (Contract # HDTRA1-08-C-0010) is gratefully acknowledged in the development and maturation of the *Ultra-High Field* ion separation technology.

References

1. Gorshkov MP (1982), USSR Inventor's Certificate No. 966,583
2. Buryakov IA, Krylov EV, Makas AL, Nazarov EG, Pervukhin VV, Rasulev UK (1991) Ion division by their mobility in high-tension alternating electric field. Sov Tech Phys Lett 17:446–447
3. Purves RW, Guevremont R (1999) Electrospray ionization high-field asymmetric waveform ion mobility spectrometry-mass spectrometry. Anal Chem 71:2346–2357
4. Miller RA, Eiceman GA, Nazarov EG (2002) A micromachined field asymmetric ion mobility spectrometer (FA-IMS). Int J Ion Mob Spectrom 5:118–134
5. Guevremont R (2004) High-field asymmetric waveform ion mobility spectrometry: a new tool for mass spectrometry. J Chromatogr A 1058:3–19
6. Petinarides J, Griffin TM, Miller RA, Nazarov EG, Bashall AD (2005) Implementation of a new technology for point detection. Proc SPIE 65:5795
7. Barnett DA, Ells B, Guevremont R, Purves RW (2002) Application of ESI-FAIMS-MS to the analysis of tryptic peptides. J Am Soc Mass Spectrom 13:1282–1291
8. Xia YQ, Steven WT, Mohammed J (2008) LC-FAIMS-MS/MS for quantification of a peptide in plasma and evaluation of FAIMS global selectivity from plasma components. Anal Chem 80:7137–7143
9. Buryakov IA (2004) Express analysis of explosives, chemical warfare agents and drugs with multicapillary column gas chromatography and ion mobility increment spectrometry. J Chromatogr B 800:75–82
10. Eiceman GA, Krylov EV, Tadjikov B, Ewing RG, Nazarov EG, Miller RA (2004) Differential mobility spectrometry of chlorocarbons with a micro-fabricated drift tube. Analyst 129:297–304
11. Krebs MD, Zapata AM, Nazarov EG, Miller RA, Costa IS, Sonenshein AL, Davis CE (2005) Microfabricated differential mobility spectrometry with pyrolysis gas chromatography for chemical characterization of bacteria. IEEE Sens J 5:696–703
12. Schmidt H, Tadjimukhamedov F, Mohrenz IV, Smith GB, Eiceman GA (2004) Microfabricated differential mobility spectrometry with pyrolysis gas chromatography for chemical characterization of bacteria. Anal Chem 76:5208–5217
13. Lambertus GR, Fix CS, Reidy SM, Miller RA, Wheeler D, Nazarov E, Sacks R (2005) Silicon microfabricated column with microfabricated differential mobility spectrometer for GC analysis of volatile organic compounds. Anal Chem 77:7563–7757
14. Cagan A, Schmidt H, Rodriguez JE, Eiceman GA (2010) Fast gas chromatography - differential ion mobility spectrometry of explosives from TATP to Tetryl without gas atmosphere modifiers. Int J Ion Mobil Spectrom 13:157–165
15. Kolakowski BM, Mester Z (2007) Review of applications of high-field asymmetric waveform ion mobility spectrometry (FAIMS) and differential mobility spectrometry (DMS). Analyst 132:842–864

16. Shvartsburg AA (2009) Differential ion mobility spectrometry. CRC Press, Boca Raton
17. Barnett DA, Ouellette RJ (2011) Elimination of the helium requirement in high-field asymmetric waveform ion mobility spectrometry (FAIMS): beneficial effects of decreasing the analyzer gap width on peptide analysis. Rapid Commun Mass Spectrom 25:1959–1971
18. Brown LJ, Toutoungi DE, Devenport NA, Reynolds J, Kaur-Atwal G, Boyle P, Creaser CS (2010) Miniaturized ultra high field asymmetric waveform ion mobility spectrometry combined with mass spectrometry for peptide analysis. Anal Chem 82:9827–9834
19. Brown LJ, Smith RW, Toutoungi DE, Reynolds JC, Bristow AWT, Ray A, Sage A, Wilson ID, Weston DJ, Boyle B, Creaser CS (2012) Enhanced analyte detection using in-source fragmentation of field asymmetric waveform ion mobility spectrometry-selected ions in combination with time-of-flight mass spectrometry. Anal Chem 84:4095–4103
20. Canterbury JD, Gladden J, Buck L, Olund R, MacCoss MJ (2010) A high voltage asymmetric waveform generator for FAIMS. J Am Soc Mass Spectrom 21:1118–1121
21. Creese AJ, Cooper HJ (2012) Separation and identification of isomeric glycopeptides by high field asymmetric waveform ion mobility spectrometry. Anal Chem 84:2597–2601
22. Rorrer LC, Yost RA (2011) Solvent vapor effects on planar high-field asymmetric waveform ion mobility spectrometry. Int J Mass Spectrom 300:173–181
23. Schneider BB, Covey TR, Coy SL, Krylov EV, Nazarov EG (2010) Control of chemical effects in the separation process of a differential mobility mass spectrometer system. Eur J Mass Spectrom 16:57–71
24. Shvartsburg AA, Prior DC, Tang K, Smith RD (2010) High-resolution differential ion mobility separations using planar analyzers at elevated dispersion fields. Anal Chem 82:7649–7655
25. Shvartsburg AA, Zheng Y, Smith RD, Kelleher NL (2012) Ion Mobility Separation of variant histone tails extending to the "middle-down" range. Anal Chem 84(10):4271–4276
26. Mason EA, McDaniel EW (1988) Transport properties of ions in gases. Wiley, New York
27. Eiceman GA, Karpas Z (2005) Ion mobility spectrometry. CRC Press, Boca Raton
28. Nazarov EG, Coy SL, Krylov EV, Miller RA, Eiceman GA (2006) Pressure effects in differential mobility spectrometry. Anal Chem 78:7697–7706
29. Boyle B, Koehl A, Ruiz-Alonso D, Rush M, Parris R, Wilks A (2008). A MEMS fabricated device for field asymmetric ion mobility spectrometry. Proceedings of the 59th Pittcon Conference, New Orleans, LA
30. Krylov EV, Nazarov EG, Miller RA, Tadjikov B, Eiceman GA (2001) Micromachined planar field asymmetric ion mobility spectrometer. Sensors Actuators A 91:301–312
31. Shvartsburg AA, Smith RD, Wilks A, Koehl A, Ruiz D, Boyle B (2009) Ultrafast differential Ion mobility spectrometry in multichannel microchips. Anal Chem 81:6489–6495
32. Krylov EV, Nazarov EG, Miller RA (2007) Differential mobility spectrometer: model of operation. Int J Mass Spectrom 266:76–85
33. Shvartsburg AA, Smith RD (2008) Optimum waveforms for differential ion mobility spectrometry. J Am Soc Mass Spectrom 19:1286–1295
34. Tamayol A, Bahrami M (2010) Laminar flow in microchannels with noncircular cross section. J Fluids Eng 132:111201
35. Krylov EV, Nazarov EG, Miller RA, Tadjikov B, Eiceman GA (2002) Field dependence of mobilities for gas-phase-protonated monomers and proton-bound dimers of ketones by planar field asymmetric ion mobility spectrometry (PFAIMS). J Phys Chem A 106:5437–5444
36. Vautz W, Bödeker B, Baumbach JI, Bader S, Westhoff M, Perl T (2009) An implementable approach to obtain reproducible reduced ion mobility. Int J Ion Mobil Spectrom 12:47–57
37. Revercomb HE, Mason EA (1975) Theory of plasma chromatography/gaseous electrophoresis. Anal Chem 47:970–983
38. Bensch H, Leonhardt M (2002) Comparison of drift times of different IMS. Int J Ion Mobil Spectrom 3:7–10
39. Tabrizchi M, Rouholahnejad F (2005) Comparing the effects of temperature and pressure on ion mobility. J Phys D: Appl Phys 38:857–867
40. Krylov EV, Coy SL, Nazarov EG (2009) Temperature effects in differential mobility spectrometry. Int J Mass Spectrom 279:119–125
41. US Department of Commerce; National Institute of Standards and Technology web book (2011), Gaithersburg. http://webbook.nist.gov/cgi/cbook.cgi?ID=B5000324. Accessed 2nd Feb 2012
42. Ewing RG, Eiceman GA, Harden CS, Stone JA (2006) the kinetics of the decompositions of the proton bound dimers of 1,4-dimethylpyridine and dimethyl methylphosphonate from atmosphere pressure ion mobility spectra. Int J Mass Spectrom 76:255–256
43. An X, Eiceman GA, Stone JA (2010) A determination of the effective temperatures for the dissociation of the proton bound dimer of dimethyl methylphosphonate in a planar differential mobility spectrometer. Int J Ion Mobil Spectrom 13:25–36
44. An X, Eiceman GA, Rodriguez JE, Stone JA (2011) Gas phase fragmentation of protonated esters in air at ambient pressure through ion heating by electric field in differential mobility spectrometry. Int J Mass Spectrom 303:181–190
45. Eiceman GA, Stone JA (2009) In: March RE, Todd JFA (eds) Practical aspects of trapped ion mass spectrometry, Volume V 387–415. Boca Raton, CRC Press
46. Stone JA (2002) The Kinetics and thermodynamics of ion solvation applicable to ion mobility spectrometry. Int J Ion Mob Spectrom 5:19–41